BACHELOR THESIS

Implementation of Digital Tomosynthesis in a Real Radiology System

Author:
Miguel Benavente Molinero

Supervisor:
Mónica Abella García

Leganés, October 10th 2016

IMPLEMENTATION OF DIGITAL TOMOSYNTHESIS IN A REAL RADIOLOGY SYSTEM

Author: Miguel Benavente Molinero

Supervisor: Mónica Abella García

Bioengineering & Aerospace Engineering Department
Universidad Carlos III de Madrid

Laboratorio de Imagen Médica (LIM)
Hospital General Universitario Gregorio Marañón

Abstract

The work included in this thesis is framed on one of the lines of research carried out by the *Biomedical Imaging and Instrumentation Group* from the *Bioengineering and Aerospace Department* of *Universidad Carlos III de Madrid* working jointly with the *Gregorio Marañón* Hospital. Its goal is to design and develop a new generation of Radiology Systems, valid for clinical and veterinary applications, through the research and development of innovative technologies in advanced image processing oriented to increase image quality, to reduce dose and to incorporate tomographic capabilities. The latter will allow bringing tomography to situations in which a CT system is not allowable due to cost issues or when the patient cannot be moved (for instance, during surgery or ICU). It may also be relevant to reduce the radiation dose delivered to the patient, if we can obtain a tomographic image from fewer projections than using a CT.

In that context, this thesis deals with incorporating pseudo-tomographic capabilities, through a tomosynthesis protocol, in a radiology room originally designed for planar images: the NOVA FA digital radiography system developed by SEDECAL. The room consists of an X-ray generator, a vertical wall stand system, a mobile elevating table and an automatic ceiling suspension which allows the X-ray source to cover the whole volume of the room. Images are acquired using a flat panel detector connected through Wi-Fi to the computer station.

Having evolved from conventional tomography, tomosynthesis produces section images at any depth from projections obtained at different angles along a linear sweep through the use of a suitable reconstruction algorithm.

A workflow was established for the incorporation of tomosynthesis protocols to the NOVA FA system starting from the design of the protocol down to the reconstruction step. This required the understanding of the system and the development of several software tools.

For the design of new protocols, a tomosynthesis module was incorporated to an in-house X-ray simulation tool programmed in Matlab and CUDA.

As the X-ray room was built specifically for research, everything is manual and all the software is open. This system is designed only for planar radiography and, as a consequence, it is very cumbersome to incorporate a protocol that involves more than one projection. Therefore, a new software tool was implemented in Matlab that allows the translation of each of the

source-detector positions corresponding to the tomosynthesis design to the geometrical parameters of the NOVA FA system and their automatic addition to its database.

To obtain a tomographic image from the data acquire, a reconstruction tool was developed in Matlab with the ability to use several reconstruction algorithms including Shift-and-Add and Backprojection.

Finally, two different evaluations were conducted: a geometric evaluation to assess the correlation between the simulation tool and the X-ray room and an evaluation of the complete workflow through the design and implementation of a simple tomosynthesis protocol using a PBU-50 body phantom developed by Kyoto Kagatu. The results of these evaluation studies showed the feasibility of the proposal.

It should be noted that the work of this thesis has a clear application in industry, since it is part of a proof of concept of the new generation of radiology systems which will be commercialised worldwide by the company SEDECAL.

Keywords

Resumen

El trabajo presentado en esta tesis forma parte de una línea de investigación llevada a cabo por el Grupo de Instrumentación e Imagen Médica del Departamento de Bioingeniería y Aeroespaciales de la Universidad Carlos III de Madrid en colaboración con el Hospital Gregorio Marañón. Tiene por objetivo el diseño y desarrollo de una nueva generación de sistemas radiológicos, con aplicación tanto en clínica como en veterinaria, a través de la investigación y el desarrollo de las nuevas tecnologías orientadas a la mejora de la calidad de la imagen, con el fin de reducir la dosis recibida por el paciente e incorporar capacidades tomográficas. Esta última característica permitiría el uso de la tomografía en situaciones en las que no es posible utilizar un sistema TAC, ya sea por razones económicas o porque el paciente no puede ser desplazado (por ejemplo, durante una cirugía o porque se encuentra en la UCI). Otro punto relevante sería la reducción de dosis de radiación recibida por el paciente, al poder obtener imágenes tomográficas usando menos proyecciones que utilizando el TAC.

En este contexto, esta tesis trata de incorporar capacidades tomográficas a través de un protocolo de tomosíntesis, a una sala de radiología, originalmente diseñado para obtener imágenes planas: el sistema de radiografía digital NOVA FA desarrollado por SEDECAL. La sala está formada por un generador de rayos X, un soporte vertical de pared, una mesa elevable y suspensión automática de techo que permite a la fuente de rayos X cubrir todo el volumen de la sala. Las imágenes son adquiridas utilizando un panel detector plano que se conecta a través de Wi-Fi a la estación de trabajo.

La tomosíntesis evolucionó de la tomografía convencional, por lo que es capaz de producir cortes tomográficos a cualquier profundidad a partir de proyecciones obtenidas desde distintos ángulos a lo largo de una trayectoria lineal mediante el uso del algoritmo de reconstrucción apropiado.

Se ha establecido un flujo de trabajo para la incorporación de protocolos de tomosíntesis al sistema NOVA FA empezando por el diseño del protocolo hasta el proceso de reconstrucción. Para ello, se ha estudiado el funcionamiento del sistema y se han preparado varias herramientas software.

Por un lado, se ha incorporado un módulo de tomosíntesis a una herramienta de simulación de sistemas de rayos X implementada en Matlab y CUDA.

La sala de rayos X fue abierta para experimentación, por lo que todo es manual y el software está abierto. El sistema está pensado sólo para radiografía y, por tanto, es muy complicado incorporar protocolos que requieren más de una radiografía. Para facilitar esta tarea, se ha implementado en Matlab una nueva herramienta de software que permite traducir cada posición fuente-detector correspondiente al protocolo diseñado a los parámetros geométricos del sistema NOVA FA y añadirlas automáticamente a la base de datos del sistema.

Para poder obtener imagen tomográfica a partir de los datos adquiridos, se ha desarrollado una herramienta de reconstrucción en Matlab con la capacidad de utilizar distintos algoritmos de reconstrucción incluyendo Shift-and-Add y Retroproyección, comúnmente usado en TAC.

Finalmente, se han llevado a cabo dos evaluaciones. Una evaluación geométrica para comprobar la correspondencia entre el simulador y la sala, y una evaluación del flujo de trabajo completo mediante el diseño e implementación de un protocolo simple de tomosíntesis con el tórax de un maniquí PBU-50 de cuerpo entero producido por Kyoto Kagatu. Los resultados de estas pruebas muestran la viabilidad de la propuesta.

Cabe destacar que el trabajo de esta tesis tiene una clara aplicación industrial, ya que forma parte de una prueba de concepto de la nueva generación de sistemas de radiología que comercializará la empresa SEDECAL en todo el mundo.

Palabras clave

Rayos X, radiografía, tomosíntesis, tomografía, imagen 3D, reconstrucción de imagen

Index of Contents

Index of Figures

Index of Tables

1 Introduction

Diagnostic imaging is a widely spread discipline in the medical world. It represents the spatial distribution of one or more physical or chemical properties inside the human body, which facilitates the detection of any anomalies in the clinical picture of a patient.

Techniques used in diagnostic imaging, also known as image modalities, are characterised by the radiation of the patient with some kind of energy. Depending on the symptoms presented, as well as the body part to be treated, doctors may apply one modality or another. Among them, radiology (X-rays), nuclear medicine (gamma γ rays), magnetic resonance imaging (radio waves), echography (ultrasound) and endoscopy (light) stand out.

Radiology is the most used medical imaging modality worldwide. It has numerous advantages such as its low cost and speed. This modality employs X-ray energy, which was discovered in 1895 by the German physician Wilhelm Conrad Röntgen who would receive the Physics Nobel prize in 1901.

1.1 Introduction to X-Rays

X-ray radiation was discovered by chance in November 1895 by Wilhelm C. Röntgen while working with a cathode ray tube. Röntgen saw that this radiation was capable of going through certain materials but not without suffering some attenuation and that it could be captured on a photographic plate similarly to light. These characteristics allowed X-rays to be utilised in medicine: the first Röntgen image was made soon after the discovery of X-rays and, a few months later, radiographs were commonplace in clinical practice.

The nature of X-rays was described by Max von Laue in 1912. X-rays are a form of electromagnetic radiation. As such, they are composed of photons whose energy E is determined by their frequency f and wavelength λ:

$$E = \frac{h \cdot c}{\lambda} = h \cdot f \qquad \text{1.1}$$

where h is Planck's constant ($4.135 \cdot 10^{-15} \ eV \cdot s$) and c is the speed of light. X-ray energy ranges from $5 \cdot 10^4$ to $10^6 \ eV$, which places X-ray radiation between ultraviolet radiation and γ rays in the electromagnetic spectrum. In medical imaging, X-ray photons usually have an energy between $10 \ keV$ and $150 \ keV$. X-rays with energies between $10 \ eV$ and $30 \ keV$, referred to as soft, are used in microscopy.

X-rays are ionizing radiation, that is, due to their high energy they are capable of stripping off electrons from atoms. Exposure to ionizing radiation can cause the rupture of molecules which can, in turn, induce chemical reactions in the organism. This is especially important in the case of water molecules due to the generation of free radicals, which are very reactive.

1.1.1 Generation of X-Rays

X-rays are produced in a vacuum tube with a cathode and an anode, known as an X-ray tube (Figure 1.2). An electric current is made to flow through a filament in the cathode causing electrons to be released through thermal excitation. A high voltage applied between the cathode and the anode accelerates the electrons toward the anode. Accelerated electrons hit the metal target (usually tungsten) in the anode, losing their energy mainly as heat and around 4% as X-ray photons.
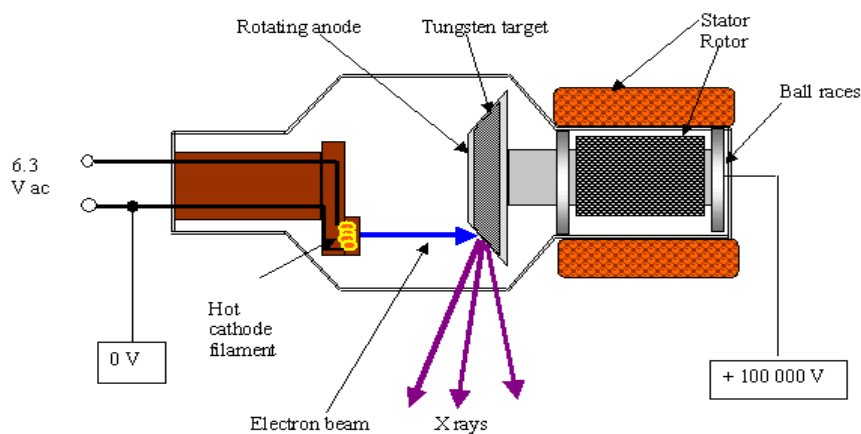
Figure 1.2 Sketch of an X-ray tube. Source: [2]

2

When electrons impact on the anode, X-ray photons can be produced by two different processes (Figure 1.3):

· Bremsstrahlung or braking radiation: it is produced when an electron passes close to an atom nucleus. Due to the positive charge of the nucleus, the incident electron changes its trajectory and slows down emitting part of its kinetic energy as an X-ray photon. This process yields a continuous X-ray spectrum. The number of photons obtained is inversely proportional to their energy.

· Characteristic radiation: this radiation is produced when an electron ionizes one of the atoms in the target material, extracting one electron from an inner layer (e.g. layer K). To fill the vacancy left by the extracted electron, an electron from an outer layer jumps to the inner one releasing part of its energy as an X-ray photon. The energy of this photon is equal to the energy difference between these two layers. Therefore, this process produces peaks in the X-ray spectrum.
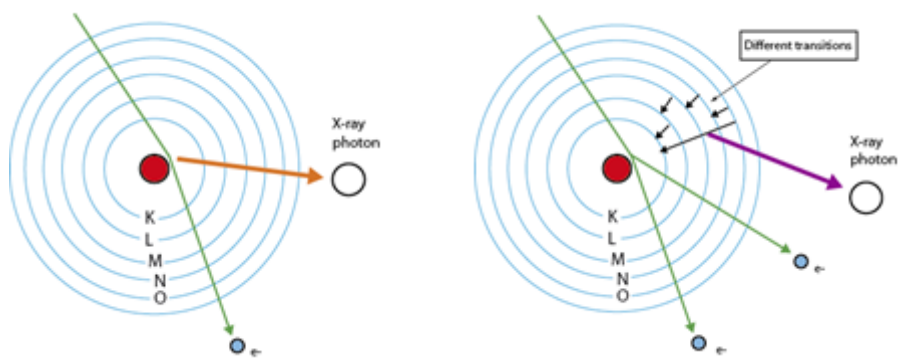
Figure 1.3 Sketch of the processes involved in X-ray generation: (left) Bremsstrahlung and (right) characteristic radiation

Low energy photons produced are absorbed within the X-ray tube, affecting the spectral distribution at low energies. The X-ray emission spectrum is displayed in Figure 1.4.
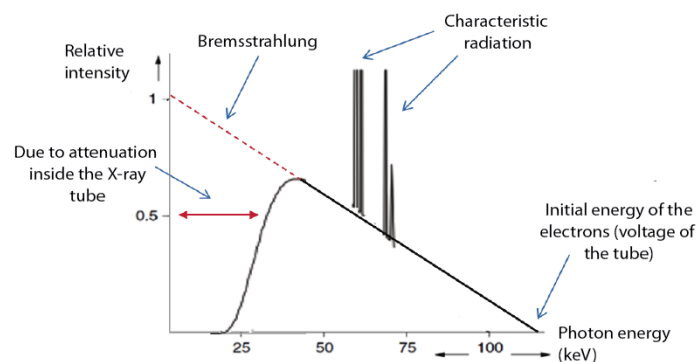
Figure 1.4 Characteristic form of the X-ray emission spectrum due to the typical phenomena that occur in the X-ray tube. Source: [3]

3

The X-ray spectrum produced by an X-ray source depends on the following parameters:

- The cathode current and the time this current is on (mAs). It determines the amount of electrons shot at the anode and, consequently, the amount of photons produced.
- The voltage applied between the cathode and the anode (kVp). It determines the energy of the electrons when hitting the anode and, consequently, the energy of the emitted photons.

1.1.2 X-Ray Interaction with Matter

X-ray photons can interact with soft tissue in three different ways due to the energy range used in diagnostic imaging $(10 - 150\ keV)$, as shown in Figure 1.5. These interactions are: Rayleigh scattering, Compton scattering and photoelectric absorption (Figure 1.6).
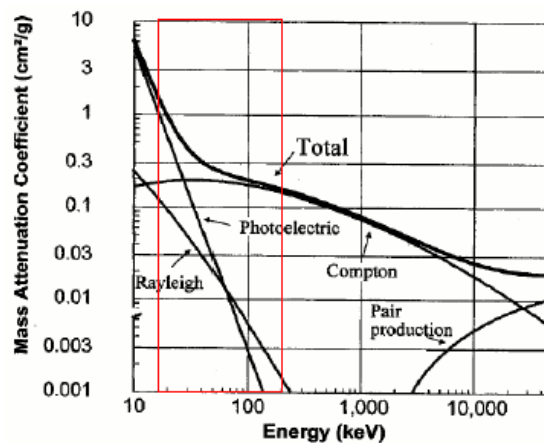
Figure 1.5 Diagram of the different phenomena produced by the interacting X-ray photons with soft tissue (photoelectric effect, Compton, Rayleigh and pair production) as a function of the energy of these photons. The red box shows the energy range (keV) used in medical imaging where photoelectric effect, Rayleigh and Compton are present. Source: [4]

- Rayleigh or coherent scattering: a photon is absorbed by an atom and immediately released in the form of a new photon with the same energy but travelling in a slightly different direction. It occurs mainly at low energies $(< 30\ keV)$.
- Photoelectric effect: an X-ray photon is absorbed, yielding its energy to an electron, which escapes from its nucleus in the same direction as the incoming photon (ionization).
- Compton scattering: an X-ray photon collides with an electron orbiting the atom, transferring only part of it energy to the electron. The electron is ejected from the atom with a certain kinetic energy, while the photon, now with lower energy, has its direction deviated.

4
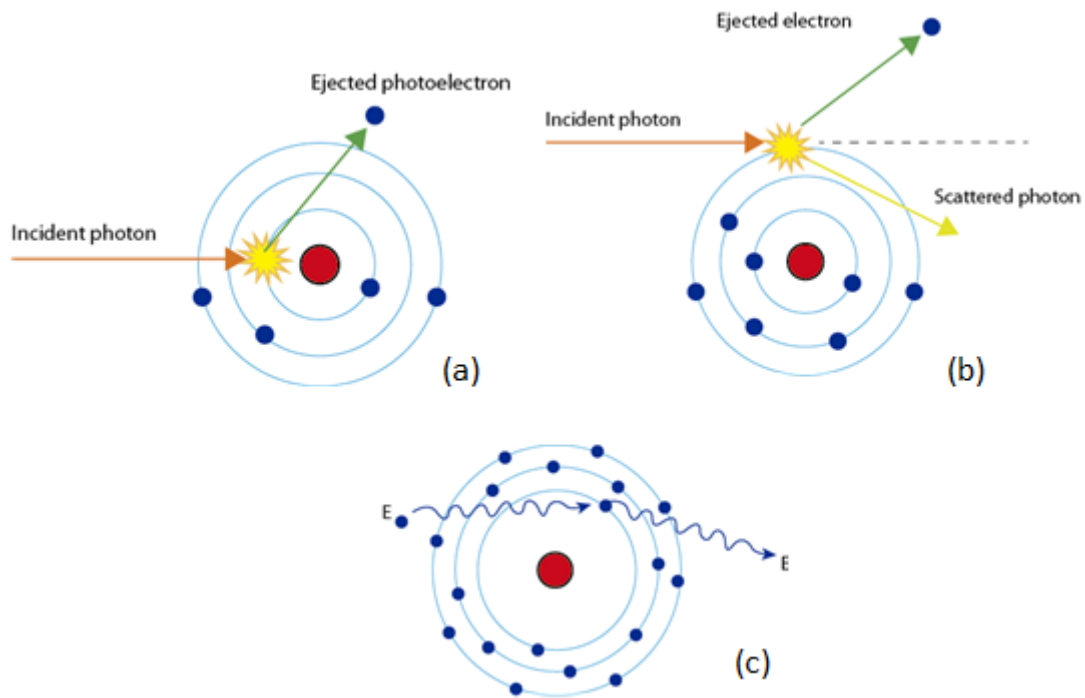
Figure 1.6 Diagrams of the processes that occur when X-ray photons interact with matter:
(a) Photoelectric effect, (b) Compton effect and (c) Rayleigh effect

1.1.3 X-Ray Detection

Initial X-ray detectors made use of photographic films covered by a silver emulsion. Since the film is more sensitive to light photons than to X-ray photons, high doses were required to obtain an image with a reasonable quality. To overcome this problem, an intensifying screen was placed in contact with the film (Figure 1.7). X-ray photons would interact with this screen producing light photons which would then be collected by the photographic film thus reducing the amount of dose required to obtain a good quality image.
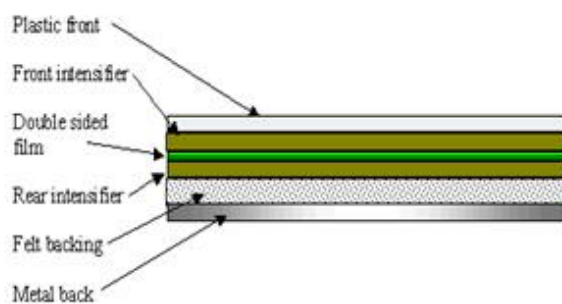
Figure 1.7 (Left) Cross section representation of a film covered on both sides by a fluorescent screen
(Right) Example of commercial intensifier screen by Soyee Product Inc. Source: [2]

The first digital systems were used in the 1980s. These systems were known as Computed Radiography (CR). The image was generated in two steps. First, the X-ray photons excite electrons in a phosphor crystal layer, temporarily storing the photon energy. This is followed

5

by a reading step: the crystal layer is forced to release the stored energy as light by exciting it with a laser. The produced light is then collected in a photomultiplier array converting it into an analogue signal which is then amplified. Finally, an analogue to digital conversion is performed. This process is summarised in Figure 1.8.
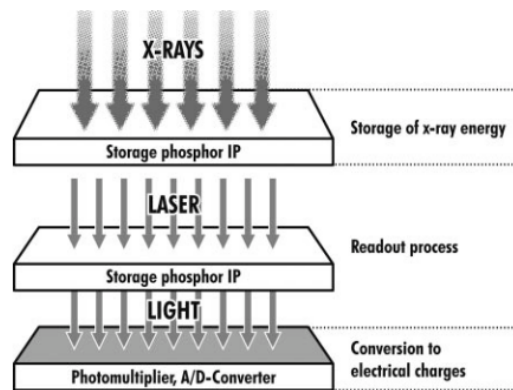
Figure 1.8 Composition diagram of a CR digital detection system. Source: [5]

The reading and conversion steps require a separate system. The incorporation of CR systems, however, was really simple as it only needed the replacement of the photographic plate by the new detector panel in the same rack.

In the 1990s, the first Direct Radiography (DR) systems appeared. These systems convert X-ray photons directly into digital signals.

DR systems can be classified as direct or indirect depending on the conversion process followed (Figure 1.9). Direct conversion systems convert X-ray photons into electric signals in a single step using a photoconductor material. Indirect conversion systems first convert X-ray photons into visible light using a scintillator; these light photons are then converted into electrical signals using a photodiode array.
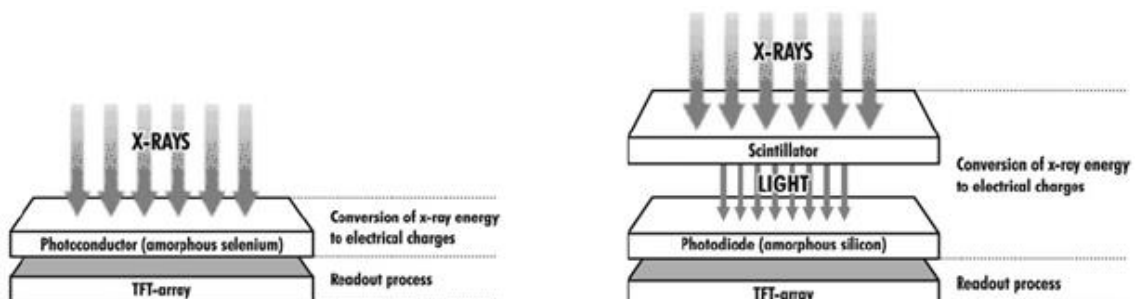
Figure 1.9 (Left) Composition diagram of a direct conversion DR digital detection system
(Right) Composition diagram of an indirect conversion DR digital detection (flat panel). Source: [5]

Flat panel detectors are one of the most common DR systems with indirect conversion. Flat panel detectors present a small size and are lighter and far more durable than other digital detectors.

1.2 X-Ray Imaging

The main imaging techniques that involve the use of X-rays are: conventional radiology, digital radiology and computerised tomography (CT). All of these techniques are ionizing as they use X-ray energy. As explained in section 1.1, X-rays induce chemical reactions in the patient due to the high energy that is being irradiated which leads to the ionization of diverse molecules. X-ray imaging allows obtaining spatial high-resolution images and the extraction of detailed information about the anatomy of the subject according to the density of the tissue traversed by the rays.

In all of these techniques, the patient stands in between an X-ray tube and a detector. The X-ray tube acts as a point source from which X-rays diverge. Because of this, structures appear larger when projected onto the detector. This increase in size is known as magnification. It depends on the distances between the source and the detector (source-detector distance SDD) and the distance between the source and the patient (source-object distance SOD) according to the following formula shown in Eq. 1.2.

$$Magnification = \frac{SDD}{SOD} \qquad\qquad \textbf{1.2}$$
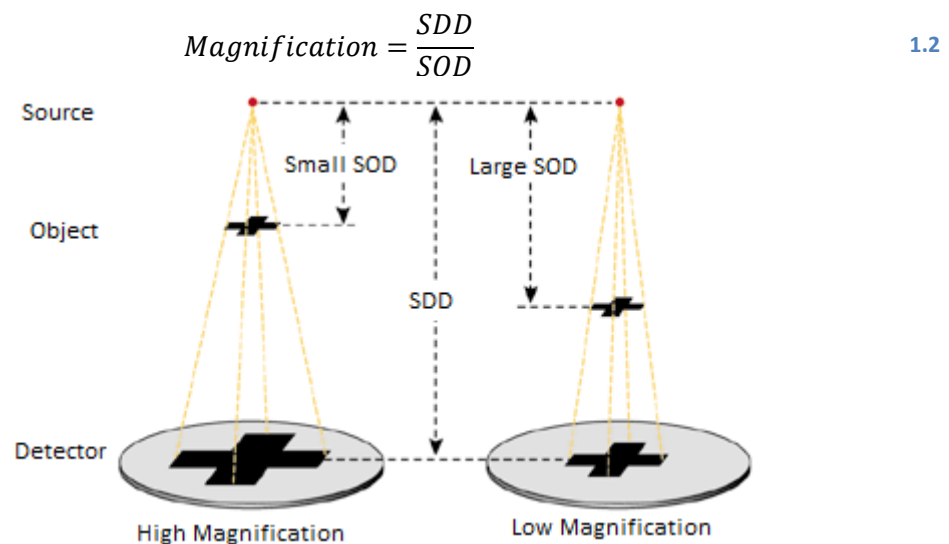
Figure 1.10 Magnification suffered by an object at different source-object distances. Source: [6]

1.2.1 Radiography

Conventional radiology is the technique by which a projective image is obtained when exposing a photographic film to radiation with high energy levels. The film captures the photons radiated by the X-ray source which were neither absorbed nor scattered by the

patient, who is placed between the source and the photographic film. These images are projective as each pixel represents the integral of the physical properties of an object along the direction of a ray being projected onto the screen.

Digital radiology is very similar to the conventional one. Its working mechanism differs only in the utilisation of a digital detector instead of the film screen, which is more sensitive and allows reducing the ionizing radiation dose to the patient. Furthermore, thanks to the digitalization of the image, it is possible to recover valid information through image processing even when the performing of the scan were not the optimal ones. Scan repetitions may be avoided when applying this technique.
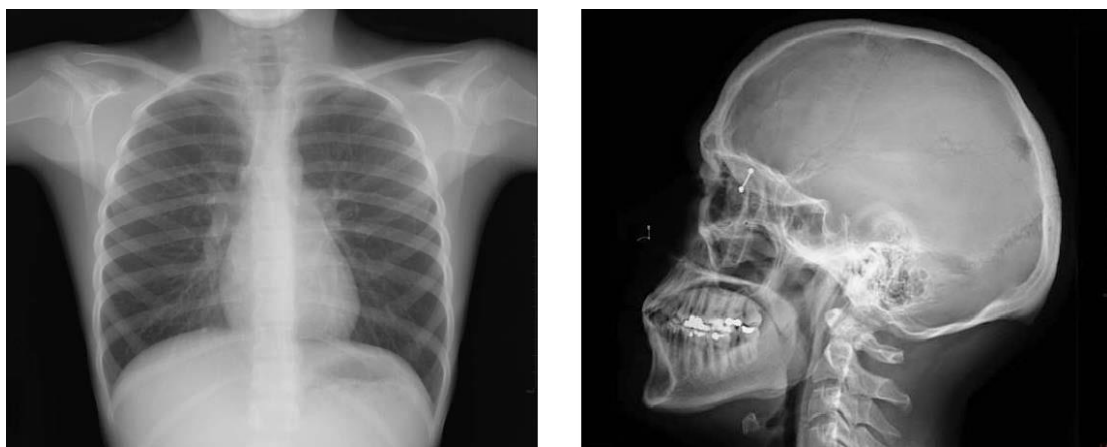
Figure 1.11 Human radiological studies: (left) thorax, and (right) cranial. Source: [7]

1.2.2 Tomography

Unlike its two predecessors, CT allows separating different planes of the sample, and representing them in two dimensional images. Tomographic slices facilitate the visualisation and interpretation of a body section without interferences from other regions (Figure 1.12).
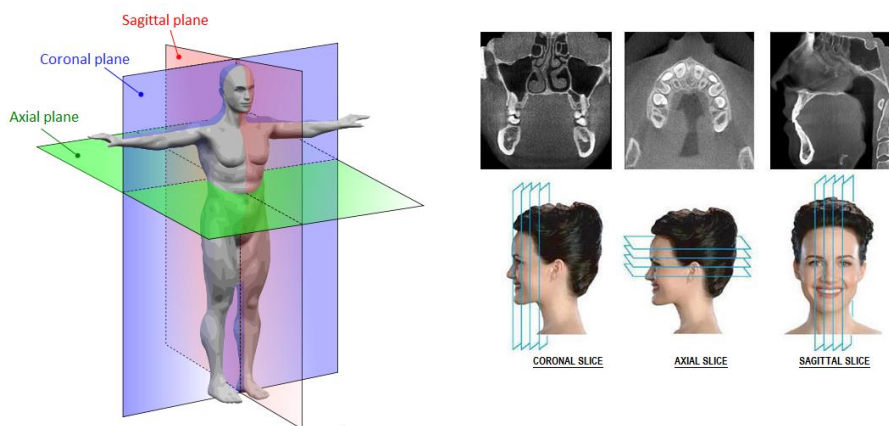
Figure 1.12 Representation of the three planes formed by tomographic slices, and (right) coronal, axial and sagittal slices from a maxillofacial CT. Source: [8]

In CT, the X-ray source and the detector rotate around the patient (Figure 1.13) taking several projections, which can then be used to reconstruct each slice. The reconstructed axial slices are then stacked thus reconstructing the whole volume scanned.
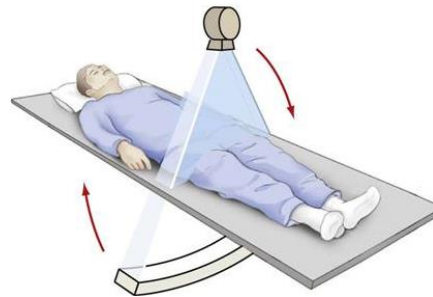
Figure 1.13 In CT, the source and the detector rotate around the patient

The Filtered Backprojection algorithm is the most common reconstruction method used in tomography systems. It allows the reconstructions of a two dimensional function from a set of one-dimensional projections acquired at many different angles around the patient. These projections are first filtered and then backprojected.

A simple example to explain the concept of backprojection is shown in Figure 1.14 using a 2D slice. In this case, only two projections were obtained: one for angle $\theta = 0°$ and one for angle $\theta = 90°$. The image backprojected for the angle $\theta = 0°$ is calculated by repeating the attenuation values accumulated for each of the horizontal rays. The backprojected image for angle $\theta = 90°$ is obtained in a similar way. The final backprojection image is the sum of the backprojected images for every angle.
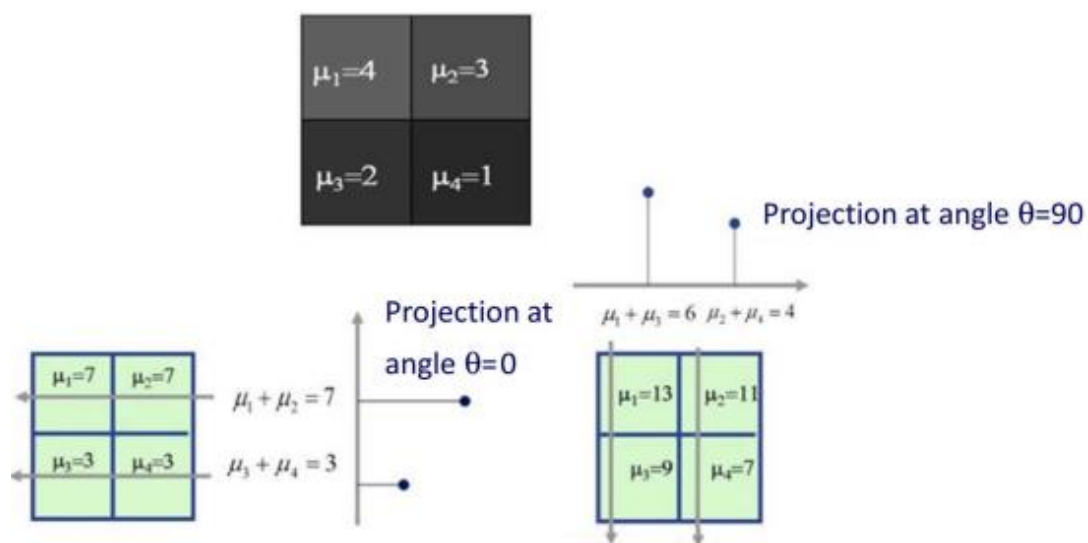
Figure 1.14 Basic example illustrating the concept of backprojection

In a real case, however, more projections are needed. These one-dimensional projections are usually arranged in a two-dimensional sinogram. Each row of a sinogram corresponds to a projection along the corresponding angle on the vertical axis.

In Figure 1.15, it can be seen that plain backprojection is not enough. If the sinogram is not filtered, the result of the backprojection is a blurred image. This implies that the low frequency component in the image is more prominent than the high frequency one. If the sinogram is filtered in the Fourier domain using a ramp filter, high frequencies are enhanced while keeping low frequencies, resulting in a better reconstruction.
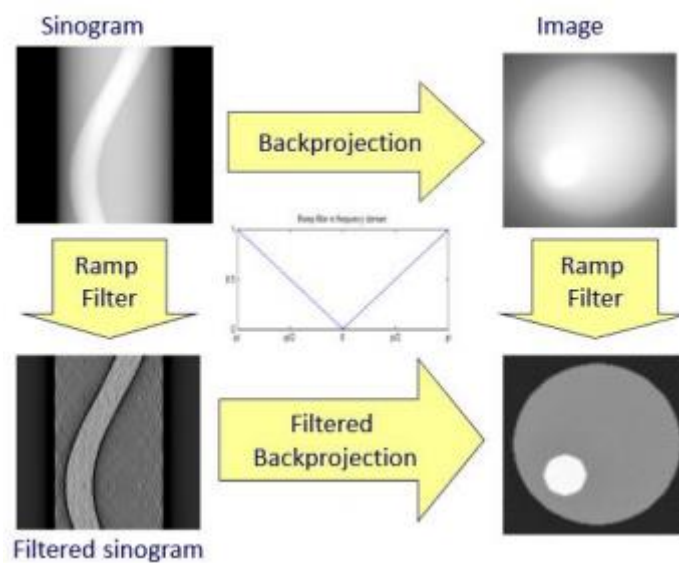
Figure 1.15 Scheme of the different steps in the FBP and the filter effect

1.3 Tomosynthesis

Tomosynthesis stands as a middle step between planar X-ray radiography and computerised tomography. Despite being a tomographic technique like CT, it is unable to completely remove the shadow of out-of-plane structures from the plane being visualised. However, this partial removal of out-of-plane structures may prove to be enough to properly diagnose the patient.

Several authors have studied the existing differences among tomosynthesis, CT and planar radiography in different applications, mostly on mammography [9-12] and chest studies [13-14]. Vikgren *et al* [14], for instance, tried comparing these modalities for chest nodule detection (Figure 1.16).

Figure 1.16 Results presented by Vikgren *et al*. From left to right: CT, radiography and tomosynthesis. Pulmonary nodules are marked in red. Source: [14]

Tomosynthesis greatly reduces the dose received by the patient when compared with CT; however, the quality of the images obtained is not as high. Thus, tomosynthesis is regarded in these studies as a promising imaging modality due to its good dose-quality ratio.

1.3.1 Digital Tomosynthesis

Digital tomosynthesis is an evolved form of traditional geometric tomography, which started appearing during the 1920s. One of its pioneers was A.E.M. Bocage, who described in 1921 a device capable of blurring out structures out of a plane of interest. This apparatus consisted on three main components: an X-ray source, an X-ray film and a mechanical connection between them that allowed for synchronous movement between them.

The principle of conventional tomography is illustrated in the Figure 1.17.
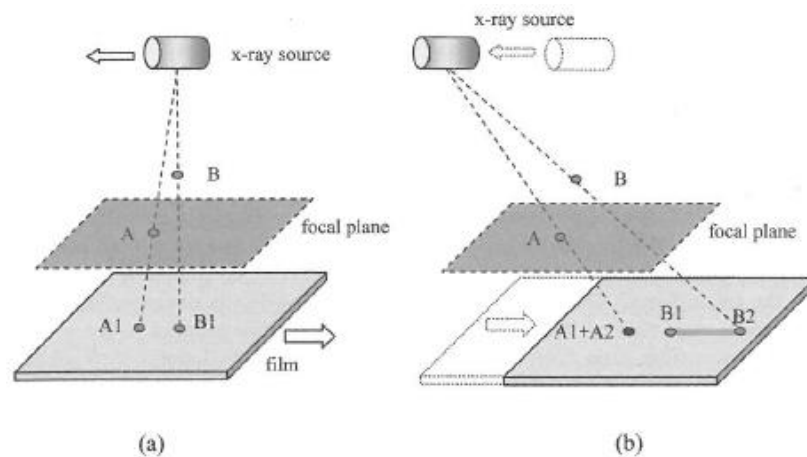
Figure 1.17 Conventional tomography principle. (a) X-ray source projects points A and B onto A1 and B1. (b) X-ray source and film are moved in such a way that shadow A2 of point A overlaps A1, but shadow B2 of point B does not overlap B1. Source: [15]

Consider two given points: A and B. The former is located within the focal plane while the latter is positioned off this plane. The acquisition then begins. First, points A and B are projected onto the film, casting their shadows at the points denoted by A1 and B1, respectively. Then, the source and the film are moved at the same time in opposite directions

until a second position is reached. The movement has been such that the shadow of point A at this second location A2 falls in the same place as A1. However, since point B does not belong to the focal plane, its shadow at this location B2 is not cast at the same position as before. Thus, unlike A1 and A2, B1 and B2 do not overlap. Since the X-ray source is emitting during the movement between both positions, point B does not only generate B1 and B2 but also a line segment connecting both points. On the other hand, point A casts its shadow at the same spot during the whole movement. Due to this property, the intensity of points out of the focal plane (represented by B) is reduced by distributing their shadows over an extended area while points within said focal plane (represented by point A) retain their position on the film, thus not having their intensity degraded and remaining in sharp focus.

While traditional tomography allowed successfully producing images at the plane of interest, it presented two main limitations:

·   Dose given to the patient: a single acquisition produced an image of a single plane; therefore, in order to image a different plane, the whole process had to be repeated, greatly increasing the dose received by the patient.
·   Inability to completely remove structures outside the focal plane: since the whole procedure only manages to blur out-of-focus structures, the contrast of the imaged focal plane is reduced.

In spite of these limitations, this technique enjoyed clinical utilization and was researched on during the following decades, earning the name tomosynthesis in the 1970s. During the 1980s, the advent of spiral CT halted much of the research in tomosynthesis.

Interest in tomosynthesis was renewed a decade later, at the end of the 1990s, due to the development of digital flat panel detectors. This new technology allowed for the reconstruction of any given number of planes from a limited number of projection images.

The advent of digital detectors also made the technique more flexible: allowing for a wider variety of possible geometries as well as a wide range of different reconstruction techniques.

1.3.2 Tomosynthesis Acquisition

In the simplest tomosynthesis geometry, the X-ray tube moves along a straight path parallel to the plane containing the receptor. The receptor may move in synchrony with the tube or remain steady depending on how close it is to the focal plane [16] (Figure 1.18). These two geometries, denoted parallel path geometries, are used mostly in acquisitions done on a table

or in front of a wall stand to image different anatomical sites such as the skull, shoulder, foot [17], or the chest [18].
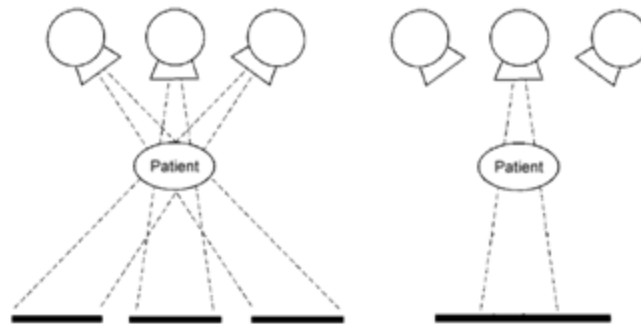
Isocentric motion is an alternative geometry [16], in which the X-ray tube and the detector rotate together around a fixed point. This is geometry used when the tomosynthesis protocol is conducted by means of devices such as the C or the U arm. Another isocentric motion, known as partial isocentric motion, has the X-ray tube moving in a similar way but the detector remains within the same plane, either moving or static. This second type of isocentric geometry is almost exclusively used in mammography [19-20]. These two geometries are shown in Figure 1.19.
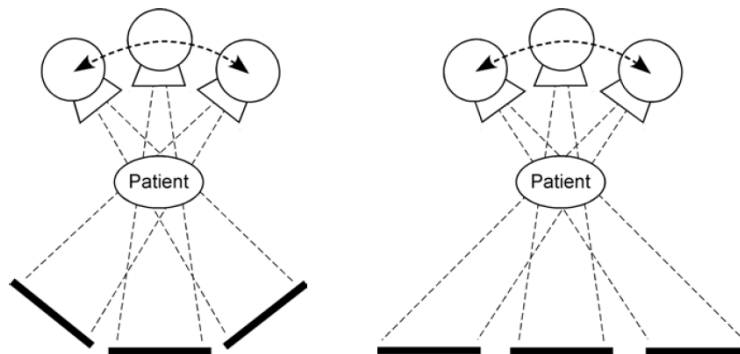
Figure 1.19 Isocentric (left) and partial isocentric (right) geometries. Source: [16]

Described geometries have the source moving within a single plane perpendicular to the detector plane. Initial studies by Xia *et al* [21] showed that having the source move along two arcs perpendicular to one another may lead to improved reconstruction quality. A similar geometry was presented by Zang and Yu [22] who also proposed rotating the detector or moving the source in zigzag. These geometries are displayed in Figure 1.20.
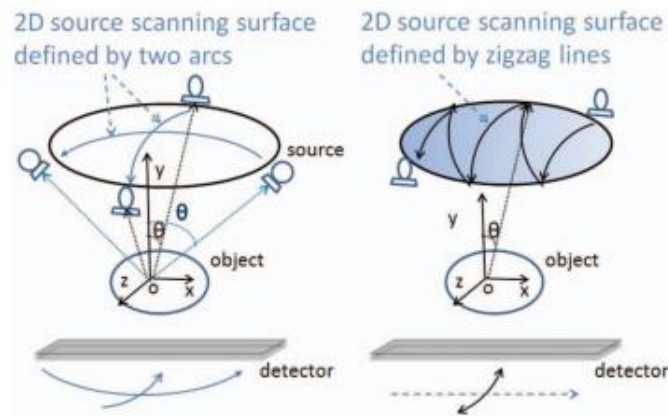
Figure 1.20 Left: geometry proposed by Xia *et al* [21] and by Zang and Yu [22]
Right: alternative geometry proposed by Zang and Yu [22]

It must be noted that the choice of geometry will have an impact on image quality. Issues arise when the detector remains stationary or moves linearly, as oblique angle incident X-ray beams on the detector will increase blurring in the image [23]. It was shown that incident angles larger than 10° have a blurring impact similar to other known sources of blurring such as focal spot penumbra. Apart from the blurring, Mainprize *et al* [23] showed that the oblique incident rays produce a small spatial shift as well that can negatively impact the reconstruction.

1.3.3 Tomosynthesis Reconstruction

SAA Algorithm

In digital tomosynthesis, the simplest reconstruction algorithm is known as Shift-and-Add [16]. Its simplest implementation is for parallel path geometries, i.e. when the X-ray tube and the detector remain within the same parallel planes during their movement. Knowing the focal plane, it is possible to find how each plane is projected onto the detector in each acquisition. This principle of this algorithm is illustrated in Figure 1.21.
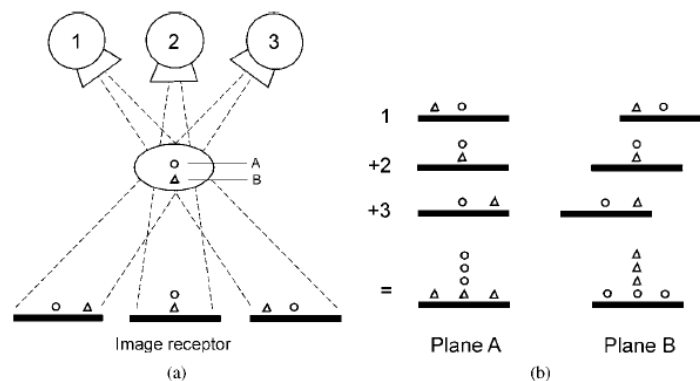
Figure 1.21 Principle of SAA algorithm. (a) Three positions of the X-ray source and the projected locations of two structures (a circle and a triangle) located in separate planes (A and B). (b) The structures in either plane can be brought into focus by shifting and adding them accordingly. Source: [16]

14

In order to better derive the Shift-and-Add algorithm, consider the geometry illustrated in Figure 1.22.
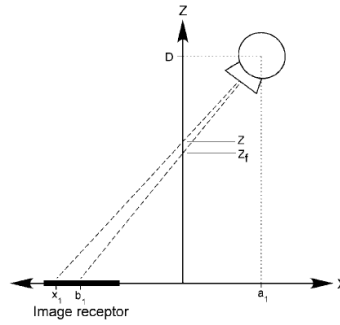
Figure 1.22 Geometry of Shift-and-Add algorithm. Source: [16]

For a given projection, the X-ray source is located at position $x = a_1$ and at a height $z = D$ and the detector is centred at $x = b_1$. The focal plane the source and the detector are moving about is located at a height z_f. In this configuration, the location of the centre of the detector is given by Eq. 1.3.

$$\frac{b_1}{z_f} = \frac{a_1}{D - z_f} \rightarrow b_1 = \frac{z_f}{D - z_f} \cdot a_1 \qquad \text{1.3}$$

A plane different from the focal one, located at a height z will be projected onto the detector with its centre falling at position x_1 which is given by Eq. 1.4.

$$\frac{x_1}{z} = \frac{a_1}{D - z} \rightarrow x_1 = \frac{z}{D - z} \cdot a_1 \qquad \text{1.4}$$

Using this formula, it is possible to know how any plane within the volume is projected in each individual acquisition. Thus, each acquisition can be shifted accordingly by an amount given by Eq. 1.5.

$$shift = x_1 - b_1 = \left(\frac{z}{D - z} - \frac{z_f}{D - z_f} \right) \cdot a_1 \qquad \text{1.5}$$

Following this shifting, the acquisitions are added bringing plane z into focus. These equations hold for arbitrary positions of the tube a_k. In general, tomosynthesis systems are designed so that the tube moves into equally spaced positions; however, it is possible to perform tomosynthesis where the tube is located at arbitrary positions.

This algorithm cannot be directly applied in isocentric configurations. Unlike in parallel path geometry, the magnification is different for each projection. That is, the same plane is

15

magnified differently for each projection. Therefore, images must be processed before applying the Shift-and-Add strategy [19]. In the case of partial isocentric motion, the basic principle for reconstruction is: knowing how the image has been projected in the isocentric geometry, and knowing how it would have been projected in the parallel path geometry, the projection obtained in isocentric geometry is converted into the theoretical projection that would have been obtained in the parallel path geometry. An example is shown in Figure 1.23. Object point (x, z) is projected to position x_i in isocentric geometry. If the it had been a parallel path geometry, it would have been projected to position x_i' (Eq. 1.6). The value of the projection at position x_i has to be moved to position x_i'. This is done with every object point.

$$\text{Isocentric Geometry} \qquad \text{Parallel Path Geometry}$$
$$x_i = z \cdot \frac{L \cdot \sin \phi + x}{L \cdot \cos \phi + D - z} \quad \leftrightarrow \quad x_i' = x + z \cdot \frac{L \cdot \tan \phi + x}{L + D - z} \qquad \qquad 1.6$$
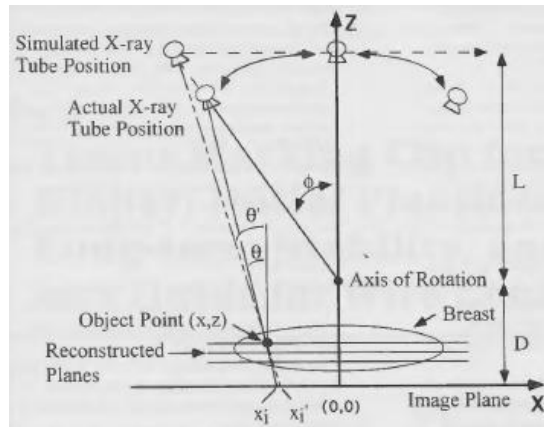
Figure 1.23 From partial isocentric to parallel path geometry. Source: [19]

Structures outside of the focal plane still appear displaced with respect to where they would be if a true parallel path geometry had been used; however, these deviations were proved to be very small and of no clinical significance [19].

In the case of pure isocentric motion, not only is magnification different in each projection, but the detector does not travel in a path parallel to any plane in the patient. Therefore, further transformations are required. These transformations were described by Kolitsi *et al* [24].

The geometry of motion used for their analysis can be is illustrated in Figure 1.24.
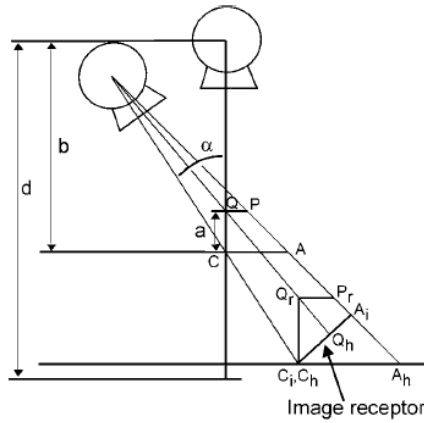
Figure 1.24 Geometric arrangement for transforming isocentric motion into planar tomosynthesis reconstruction. Source: [16]

The source and the detector rotate around the isocentre C. Line segment CA located at the plane of interest (which contains the isocentre) is projected on the detector as segment $C_i A_i$. In order to reconstruct this plane, the projected data $C_i A_i$ must be converted to a horizontal surface $C_h A_h$ parallel to the plane of interest. Kolitsi *et al* do this conversion by means of Eq. 1.7.

$$h = \frac{id}{d \cos \alpha - i \sin \alpha}$$

<div align="right">

1.7

</div>

where h is the distance from the origin C_h in the horizontal plane, and i is the distance from the origin C_i in the image receptor plane. These origins C_h and C_i are the projected points of the isocentre C. As Figure 1.24 suggests, this transformation implies a stretching of the data obtained. Kolitsi *et al* [24] also showed that for any angle α, the projected distance $C_h A_h$ in the horizontal plane is constant; therefore, no distortion of the projected segment CA is produced as a function of angle. Thus, after applying the transformation given by the equation, a series of projection images may be added to bring a plane passing through the isocentre C into focus.

Kolitsi *et al* [24] demonstrated that this method can be extended to reconstruct planes that do not cross the isocentre. Additionally, this method can also be applied to reconstruct planes in any given orientation, unlike previous algorithms shown which can only reconstruct planes parallel to the detector.

Due to its simplicity, SAA forms the basis for most tomosynthesis algorithms. One example is tuned aperture computed tomography TACT described by Webber *et al* [25]. This method allows acquiring images from random positions and then reconstructing any given plane by means of fiducial markers that must be placed beforehand on the volume to be imaged.

SAA, however, is similar to plain backprojection [26]. Thus, despite its simplicity, low quality reconstructions are obtained due to the presence of blurring from out of focus planes. In order to improve the quality of the reconstruction, a deblurring algorithm must be applied.

One of the most commonly used deblurring algorithm is filtered backprojection, also used in CT. While in CT data is acquired over a 2D area, tomosynthesis acquires projections over a 3D volume; as such, filtering is performed in 3D Fourier space domain [16]. The choice of filter greatly influences the final result [27]. The Feldkamp, David and Kreis (FDK) algorithm developed by Feldkamp *et al* [28] initially for CT was implemented for its use in tomosynthesis for image guided radiation therapy by Park *et al* [29]. Thanks to their implementation of FDK using a GPU, reconstruction of a $512 \times 512 \times 256$ volume was accomplished in less than 3 seconds.

Selective plane removal is a different deblurring algorithm developed by Ghosh Roy *et al* [30]. This method finds a blurring function from planes adjacent to the plane of interest. This blurring function is then subtracted from the plane of interest.

Dobbins *et al* [16,31] developed the matrix inversion tomosynthesis MITS deblurring algorithm based on the work of Ghosh Roy *et al* [30]. This algorithm uses linear algebra to remove the blurring in each of the reconstructed planes. While FBP deals better with noise at low frequencies, MITS deals better with noise at high frequencies [26]. Therefore, Dobbins *et al* [16, 26, 31] have shown interest in combining both methods so as to improve noise response.

Iterative Algorithms

Several iterative algorithms are described in the literature, most of which were reviewed by Colsher [32]. Algebraic iterative methods described by Colsher include: algebraic reconstruction technique (ART), simultaneous iterative reconstruction technique (SIRT) and iterative least squares technique (ILTS). The basis for these methods is the same: project an estimate of the densities of the volume and compare the results with the real projections; then, use the error to correct the initial estimate through backprojection. The methods differ on how the error is computed. An updated version of ART known as simultaneous algebraic reconstruction technique (SART) was described by Andersen *et al* [33].

Iterative reconstruction methods based on statistics also exist. In digital breast tomosynthesis, for instance, the maximum likelihood expectation maximization (MLEM) method is widely used [27]. The objective of this algorithm is to maximize the probability of getting the measured projections from an estimation of the volume.

Comparison of Reconstruction Methods

Several authors compare the wide variety of reconstruction techniques in order to find the most suitable ones for different applications. Several algorithms have been compared, e.g., for breast tomosynthesis [34-35]: BP, FBP, SART and maximum likelihood (ML). BP yielded a reconstruction with interplane artefacts that significantly blurred the reconstructed planes. FBP was found to be the best for detecting large calcifications, but failed for smaller ones. SART and ML yielded the best results, presenting good contrast for both calcifications and soft tissue. However, ML required more iterations than SART to yield similar results.

1.3.4 Potential Undesirable Effects in Tomosynthesis

Blurring-Ripple

Blurring occurs along the sweep direction and is due to the imaging of structures outside of the section plane. All objects outside the focused plane are blurred; however, the artefact is more prominent for high contrast structures that lie perpendicular to the sweep direction (Figure 1.25). The incomplete removal of the contrast of out-of-plane structures is due to the limited sweep angle used in tomosynthesis.
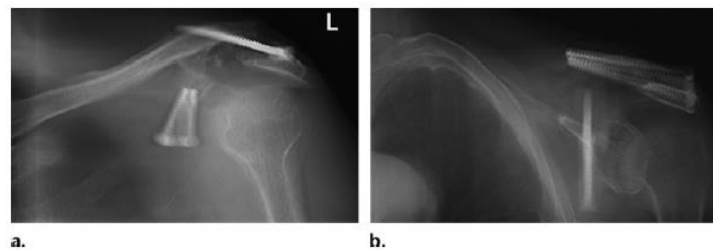
Figure 1.25 Blurring. Digital tomosynthesis of a shoulder obtained with a horizontal (a) and vertical (b) sweeps. Source: [17]

A similar mechanism also causes the ripple artefact (Figure 1.26). It is caused by a high contrast structure which is far away from the plane being focused and its contribution to this plane is not sufficiently blurred. In other words, the distance between consecutive projections is wider than the tomographic blurring. Thus, blurring changes into ripple as the perpendicular distance from the ripple source increases.
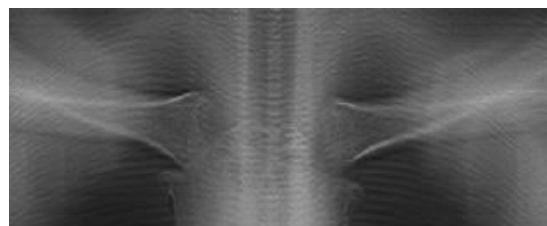
Figure 1.26 Ripple artefact caused by dorsal ribs located far from shown plane. Source: [17]

The ripple artefact can be reduced or even completely removed by increasing the projection density during the acquisition as shown in Figure 1.27.
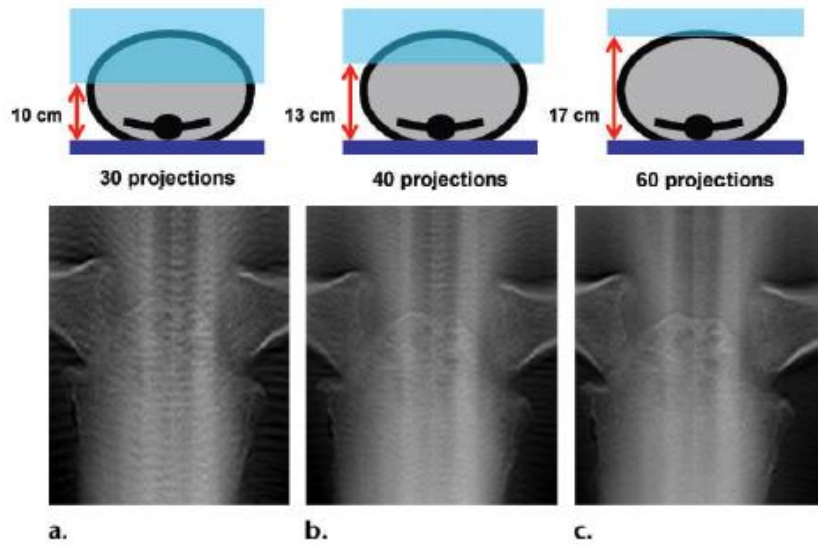
Figure 1.27 Digital tomosynthesis images of a chest phantom obtained 15 cm above dorsal ribs with 30 (a), 40 (b) and 60 (c) projections prove that the area where ripple occurs (blue shaded area) is reduced. Source: [17]

Ghost Artefact - Distortion

Little to no blurring occurs along the direction perpendicular to the sweep direction. As a result, objects whose long axis is parallel to the sweep direction only appear to be elongated along the direction of motion giving no information about their relative depth and thus appear in the final reconstruction in planes they do not belong to as ghost artefacts (Figure 1.28).
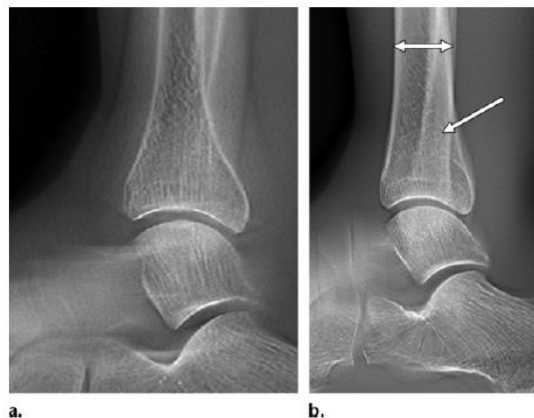
Figure 1.28 Ghost artefact. Digital tomosynthesis image of a leg phantom obtained with a sweep direction perpendicular (a) and parallel (b) to the long axis of the tibia. The fibula is insufficiently removed in (b), appearing as a ghost artefact. Source: [17]

Due to this same mechanism, when the sweep direction is oblique with respect to a given object, the object can appear distorted in the reconstruction.

Poor Spatial Resolution

Two different spatial resolutions can be identified in tomosynthesis: in-plane resolution and depth resolution. Similar to conventional radiography, in-plane resolution depends mainly on the resolution of the detector used. Due to magnification, the distance to the detector also affects in-section resolution.

On the other hand, depth resolution depends on the sweep angle. In particular, it has been shown that increasing the sweep angle decreases slice thickness thus increasing depth resolution. More specifically, slice thickness $s.t.$ has been found to be inversely proportional to the tangent of half the sweep angle α (Eq. 1.8).

$$s.t. \propto \frac{1}{\tan {\alpha}/{2}} \qquad \qquad \text{1.8}$$

Patient barrier-object distance can also affect depth resolution. Increasing this distance is equivalent to increasing the sweep angle as the incident angle is widened. This can be seen in Figure 1.29.
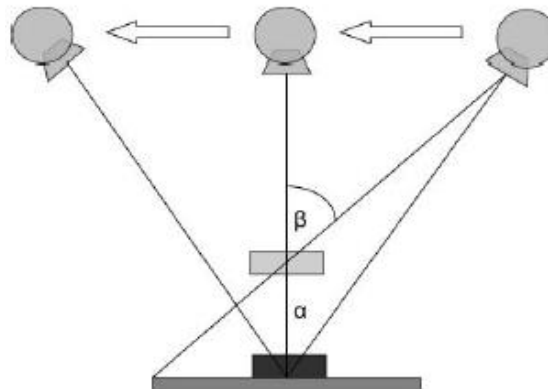
Figure 1.29 Increasing the patient barrier-object distance increases the angle of incidence from α to β. Source: [17]

Image Noise

Image noise depends on total radiation dose, as proved by Deller *et al* [36]. Total dose can be changed in two ways: either by increasing the dose per acquisition or by increasing the number of projections. Deller *et al* [36] also showed that the former strategy has a more noticeable impact on reducing noise tan the latter.

In any case, the ALARA principle (as low as reasonably achievable) establishes a limit to how much dose can be increased. That is, the dose must be the minimum required for achieving sufficient image quality.

Metallic Artefact

The metallic artefact is the appearance of very low signal along the sweep direction around the edges of a high attenuation material such as metallic prostheses. When compared to the same artefact in CT and MRI, the degree of this artefact is minimal (Figure 1.30).
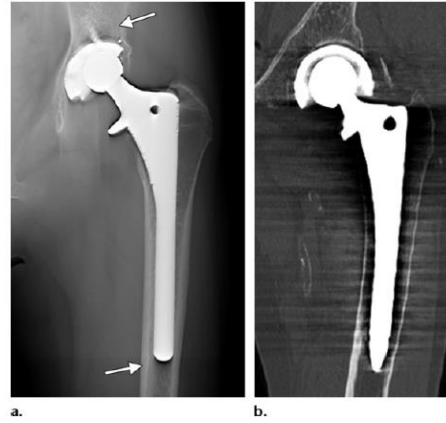
Figure 1.30 Metallic artefact in tomosynthesis (a) and CT (b). Source: [17]

2 Motivation & Objectives

2.1 Motivation

In the area of radiological technologies, recent years are seeing a rapid advance towards digital equipment. The introduction of digital detectors in conventional radiology systems not only allows an easier handling of imaging studies with PACS (Picture Archiving and Communication System), but also opens the door to a revolution in the field of so-called "Conventional" Radiology. This digitalization raises the opportunity of using advanced processing methods that convey significant advantages compared to previous technology, especially in terms of increasing the contrast and dynamic range of images and, more interestingly, of obtaining studies in which the third spatial dimension is included. The latter will allow bringing tomography to situations in which a CT system is not available due to cost issues or when the patient cannot be moved (for instance, during surgery or ICU). It may also be relevant to reduce the radiation dose delivered to the patient, if we can obtain a tomographic image from fewer projections than using a CT. With this revolution, radiology equipment, which currently accounts for over 80% of imaging studies in the clinic, will have an even more important role in the near future for both the patient and the health system.

On the other hand, in the US, there is a big social concern with the dose delivered to the patient, particularly important in paediatrics, which is creating a new regulation in this area with the aim of reducing to the minimum possible value the dose in radiological studies, according to the ALARA principle ("As Low As Reasonably Achievable"). Although this emphasis on reducing this dose received by the patient is not yet evident in Europe, extrapolating the trend in the US, we can expect to have an increasing (and reasonable) pressure in order that imaging systems use the lowest possible dose.

The work included in this thesis is framed on one of the lines of research carried out by the *Biomedical Imaging and Instrumentation* group from the *Bioengineering and Aerospace Department of Universidad Carlos III de Madrid* working jointly with the *Gregorio Marañón Hospital* through its *Instituto de Investigación Sanitaria*. This line of research is conducted in collaboration with the company SEDECAL and has a clear orientation towards the technology transfer to the industry. Its goal is to design and develop a new generation of Radiology Systems, valid for clinical and veterinary applications, through the research and development of innovative technologies in advanced image processing oriented to increase image quality, to

reduce dose and to incorporate tomography capabilities. In that context, this thesis deals with incorporating tomographic capabilities in a radiology room, originally designed for planar images.

The work of this thesis is based on the SEDECAL NOVA FA digital radiography system located at *Universidad Carlos III*. The NOVA FA system consists of a mobile elevating table, a vertical wall stand system and an automatic ceiling suspension, which allows the X-ray source to cover all the volume of the room in which the system is installed. This advanced radiology room was built specifically for research. Therefore, everything is manual and all the software is open.

Figure 2.1 NOVA FA digital radiography system

2.2 Objectives

The general objective of this thesis is to implement tomosynthesis capabilities in the NOVA FA digital radiography system. In order to meet this objective, the thesis was divided into the following tasks:

1. Preparation of a simulation tool for the design of tomosynthesis protocols
2. Automatization of the incorporation of new protocols to the NOVA FA system
3. Setup of a tomosynthesis reconstruction tool
4. Evaluation of the complete workflow for the implementation of tomosynthesis

2.3 Outline of the Manuscript

The manuscript is comprised of the following chapters:

- **Chapter 1: Introduction**. The physical basis of X-rays is described including generation, interaction with matter and detection as well as the differences between planar X-ray, CT and tomosynthesis. An introduction to tomosynthesis is provided including historical background, possible geometries, reconstruction algorithms and possible undesirable effects.
- **Chapter 2: Motivation & Objectives**. This chapter describes the line of research in which this thesis is included and the specific objectives.

- **Chapter 3: Main Contributions of the Thesis.** In this chapter, it is described how the workflow for the incorporation of tomosynthesis protocols to the NOVA FA system was established. This includes the preparation of a protocol design tool and of a reconstruction tool as well as the automatization of the incorporation of protocols to the system.

- **Chapter 4: Evaluation.** In this chapter, the evaluation of the complete tomosynthesis workflow done is described.

- **Chapter 5: Conclusions & Future Work.**

- **Chapter 6: Project Management.**

3 Main Contributions of the Thesis

A workflow was established for the implementation of tomosynthesis protocols to the NOVA FA system starting from the design of the protocol down to the reconstruction step. This required the development of several software tools which are described in detail in this chapter.

In the first section, a description of the simulation tool used for the design of acquisition protocols is given as well as the procedure followed to set it up for this thesis. The second section describes the NOVA FA radiology system, detailing the software tools used to interact with it and outlines the Matlab program that was developed for the automatization of the incorporation of new protocols. Finally, the third section presents the reconstruction tool that was implemented for the reconstruction of tomosynthesis acquisitions. The chapter ends with a description of the complete workflow for the incorporation of tomosynthesis protocols which makes use of all the tools described.

3.1 Tomosynthesis Protocol Design Tool

The first step for the implementation of tomosynthesis to the NOVA FA system is the design of the protocol itself. This was done based on an existing software tool for the simulation of X-ray acquisition protocols by incorporating a tomosynthesis module.

3.1.1 Simulation Tool

The X-ray simulator is a software tool that makes the design of X-ray acquisition protocols possible [37]. It can, therefore, be used to assess the viability of the implementation of new protocols in specific real systems.

Through a graphical user interface, it allows defining flexible projection geometries for any X-ray system configuration. The software provides a preview of simulated projections through GPU-accelerated kernels, the scanned field of view (FOV) and the estimation of the total radiation dose to allow the evaluation of the protocol in real time.

The tool is mainly implemented in Matlab. The simulated projections are formed following the Beer Lambert law:

$$I = \sum_k I_0(\varepsilon_k) \cdot e^{-\sum_i mac_i(\varepsilon_k) \int_L \rho_i dL} \tag{3.1}$$

Where $I_0(\varepsilon_k)$ is the energy spectrum, mac_i and ρ_i are the mass attenuation coefficient and

density map of material i, respectively. The term $\int_L \rho_i dL$ is obtained by a geometrical projection kernel implemented in CUDA, benefitting from GPU acceleration techniques. The energy spectrum, mass attenuation coefficients and density thresholds for each material are provided in text files along with the volume data.

The interface of the simulation tool is shown in Figure 3.1.
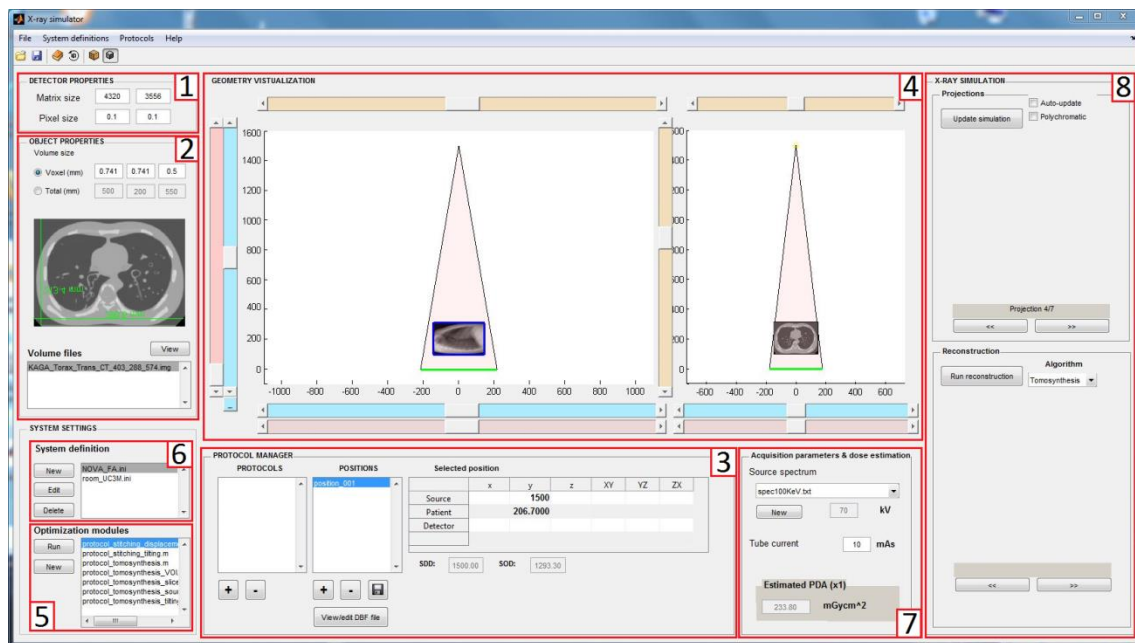
Figure 3.1 Graphical user interface for the simulation tool

In the *Detector Properties* panel (panel 1), the user may introduce the size of the detector and its pixel size in millimetres. In the *Object Properties* panel (panel 2), the volume to be imaged is loaded. This volume may be a synthetic one or a CT scan obtained from a real volume.

Acquisition protocols are defined as a set of positions defined by the placement and orientation of the X-ray source, patient and detector in the acquisition system. The user may create new protocols both manually and automatically.

Protocols are manually created, edited and managed using the *Protocol Manager* panel (panel 3). Positions to be included in the protocol are shown in the *Positions* list. Positions may be added or deleted using the plus and minus buttons underneath this list. Each position can be edited by selecting it in the list and then modifying its parameters in the *Selected Position* table. These positions, together with the loaded volume, can be visualised in the two displays (*zy* and *xy* views, respectively) in the *Geometry Visualization* part (panel 4). Once the user is satisfied with the positions created, the protocol is created using the *Protocols* list and the buttons underneath it.

Protocols may be automatically generated using the *Optimization Modules* list (panel 5), which allows the use of predefined protocols according to a set of parameters introduced by the user. The tool will then compute the positions and load them in the *Positions* list in the *Protocol Manager* panel. The user may then edit these positions further as explained before.

In the *Acquisition parameters & dose estimation panel* (panel 7), the source spectrum, kV and mAs are set. This panel also shows dose estimation.

The *X-ray Simulator* panel (panel 8) displays the simulated projections.

If a *system definition* file is available (selected in panel 6), the tool will translate these positions into the system of coordinates employed by the real system.

3.1.2 Incorporation of a Tomosynthesis Module

During this thesis a tomosynthesis module was implemented using Matlab and incorporated to the *Optimization Modules* list of the simulation tool.

The first step for designing the tomosynthesis module was to determine which are the most important acquisition parameters in a tomosynthesis protocol. Checking the literature [17], it was seen that the most important parameters are:

· The number of projections taken along the movement of the source (Figure 3.2)

· The height at which the focal plane is placed (Figure 3.2)

· The maximum source displacement (Figure 3.2)

· The field of view (Figure 3.3)

· The slice thickness (Figure 3.4)
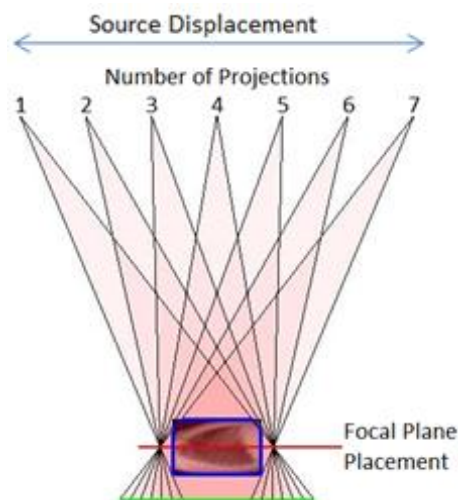
Figure 3.2 Number of projections, focal plane placement and maximum source displacement

28

The field of view of any tomosynthesis acquisition protocol is the volume of space that can be seen by every projection in the protocol. It depends both on the maximum source displacement and the focal plane placement.
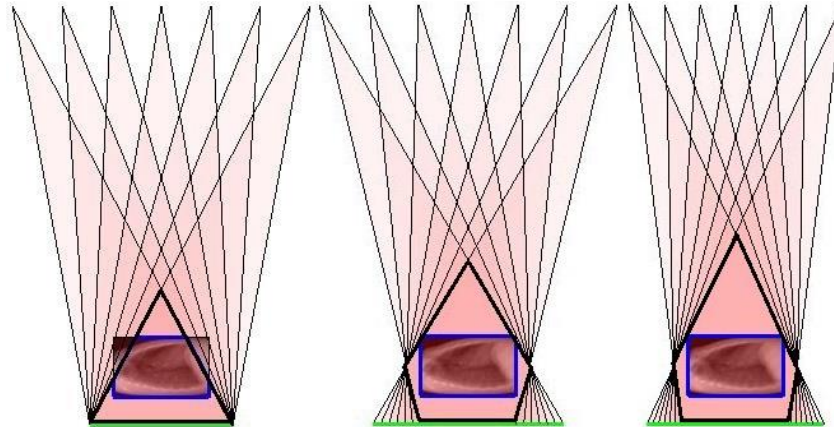
Figure 3.3 Tomosynthesis FOV for different focal plane placement and maximum source displacement
In black: FOV of the protocol
In blue: part of the volume within the FOV

The slice thickness is related to the resolution of the reconstruction. The resolution in the *x* and *y* directions is determined by the detector resolution. The resolution in the *z* direction is referred to as slice thickness. This thickness, st, depends on the angle α, known as sweep angle, shown in Figure 3.4. Therefore, it depends on the source displacement.

$$st \propto \frac{1}{\tan{\alpha}/2} = \frac{source - object\ distance}{\frac{1}{2} \cdot source\ displacement} \qquad \text{3. 2}$$
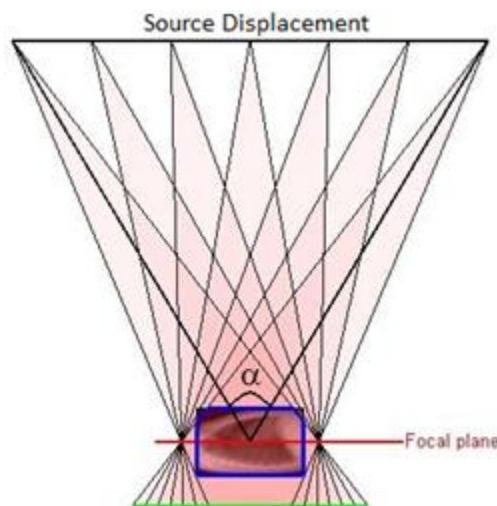
Figure 3.4 Angle α covered by a tomosynthesis protocol

While the number of projections and the placement of the focal plane are independent, the remaining three parameters are related; that is, setting one of these parameters determines the other two. As a result, the tomosynthesis module consists of three different submodules or entries in the *Optimization Modules* list.

In the first submodule (Figure 3.5), the user may choose the number of projections, the placement of the focal plane and the maximum displacement of the source. The program will then calculate the source-detector positions that fulfil these requirements as well as the resulting slice thickness (using Eq. 3.2), disregarding whether or not the loaded volume fits within the field of view.
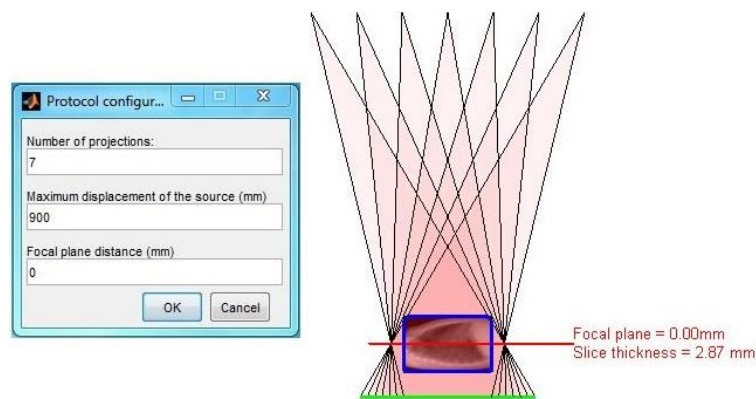
Figure 3.5 Example of input (left) and output (right) for the maximum source displacement tomosynthesis module

In the second submodule (Figure 3.6), the user first introduces the number of projections. Then, they must indicate which part of the loaded volume they are most interested in. The user may choose the whole volume or draw a smaller region within the loaded volume. Then, placing the focal plane in the middle of the chosen VOI, the program will find the maximum source displacement that keeps the VOI within the field of view. Finally, source-detector positions are shown as well as the slice thickness.
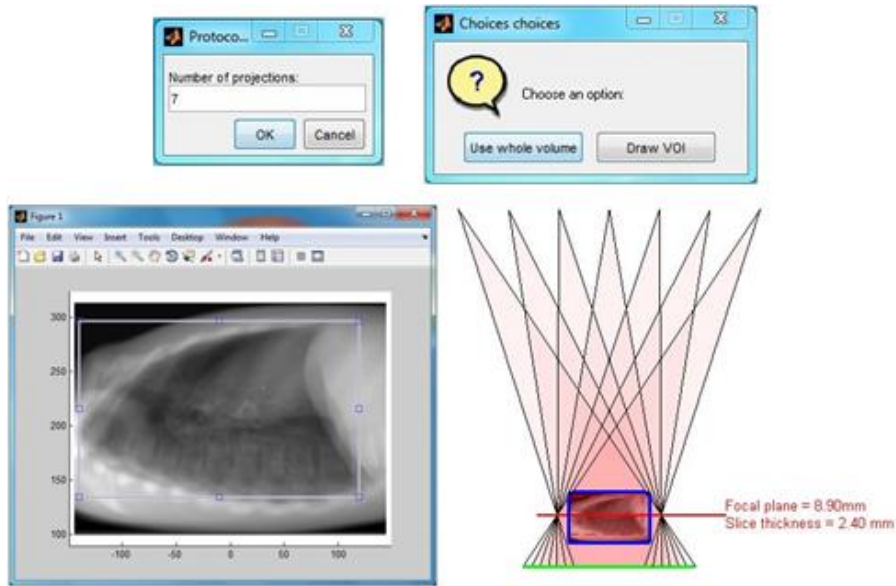
Figure 3.6 Example of input and output for the VOI tomosynthesis module.The user first introduces number of projections (top left) and then decides which is the VOI (top right). Using the *Draw VOI option*, the user may decide which part of the volume is the VOI (bottom left). The module then produces an acquisition protocol (bottom right)

In the third submodule (Figure 3.7), the user may choose the number of projections, where to place the focal plane and the slice thickness desired. The software will then find the maximum displacement of the source (using Eq. 3.3) and, finally, yield the source-detector positions that ensure the introduced slice thickness is achieved. Whether the loaded volume fits within the resulting FOV is disregarded.

$$source\ displacement = 2 \cdot \frac{source - object\ distance}{slice\ thickness}$$ 3. 3
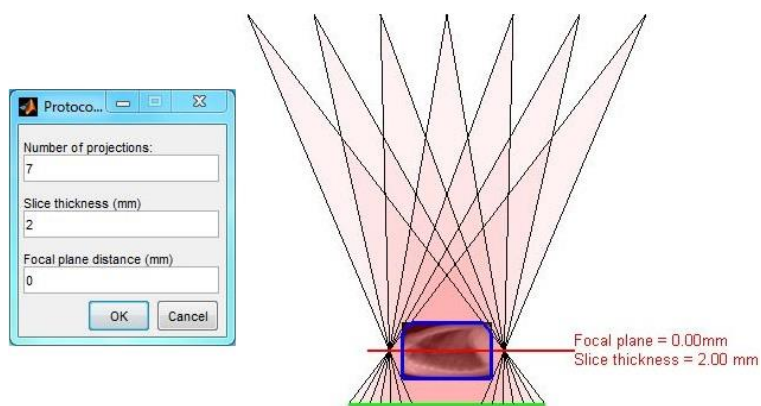
Figure 3.7 Example of input (left) and output (right) for the slice thickness tomosynthesis module

31

3.2 Incorporation of Tomosynthesis to the NOVA FA System

The tomosynthesis protocol designed had then to be implemented in the SEDECAL NOVA FA digital radiography system located at *Universidad Carlos III*. This advanced radiology room was built specifically for research. Therefore, everything is manual and all the software is open.

In this section, the NOVA FA system is described including the software tools used to interact with it. Although it is possible to use these tools to incorporate multi-position protocols manually, this is unpractical when dealing with protocols with a large amount of projections, as is the case with tomosynthesis. Therefore, an alternative automatic method was proposed during this thesis.

Finally, the Reconstruction Tool implemented during this thesis is described.

3.2.1 The NOVA FA Radiography System

The SEDECAL NOVA FA digital radiography system used in this thesis is located at *Universidad Carlos III* (Figure 3.8). This system consists of a mobile elevating table, a vertical wall stand system and an X-ray generator. Floor space is freed up by suspending the X-ray tube and collimator together with a telescopic tube support column, running gear and high tensions cables. This is known as the ceiling suspension and it can move the X-ray tube all around the room allowing acquisitions both at the wall stand and at the table.

Figure 3. 8 NOVA FA digital radiography system

By communicating with the ceiling suspension, it is possible to remotely move the elements in the room. Communication is established through the Secure Shell (SHH) protocol using Putty, which then opens the Suspension Tool shown in Figure 3.9. Graphical interface support is provided by Xming, the X Window System display server, which provides a set of traditional sample X applications and tools.
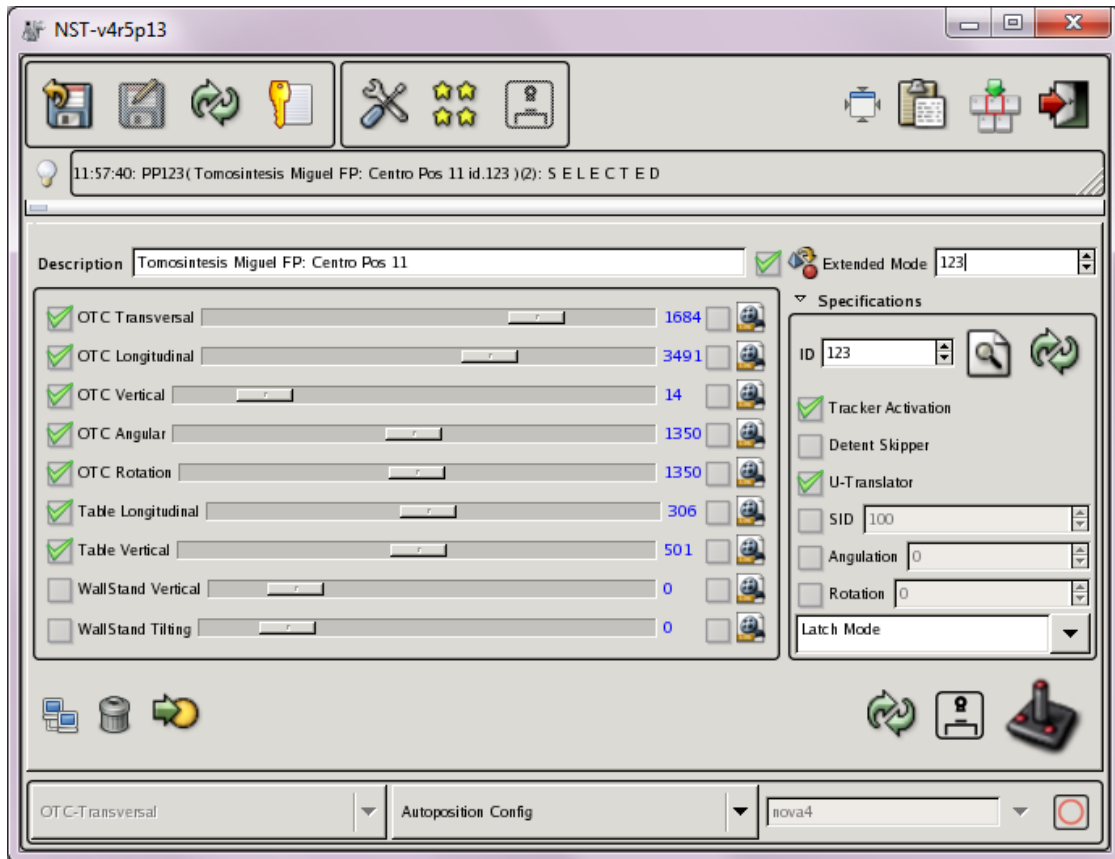
Figure 3.9 Suspension Tool

Using this tool the user can move all three elements in the room: source, table and wall stand. The position of the source, referred to as *OTC* by the interface, is defined using 5 parameters corresponding to displacement along three axes (*transversal*, *longitudinal* and *vertical*) and two rotations (*angular* and *rotation*).

The position of the table, referred to as *Table* in Figure 3.9, is defined using two parameters. The first one corresponds to the position of the detector within the table (*longitudinal*). The second one refers to the height at which the table is located (*vertical*). This second parameter is the only one that cannot be controlled remotely and must be set manually.

The position of the wall stand, referred to as *WallStand* in Figure 3.9, is defined by two parameters, which refer to the height it is at (*vertical*) and its angulation (*tilting*).

How each parameter relates to the placement of the elements of the system is shown in Figure 3.10.
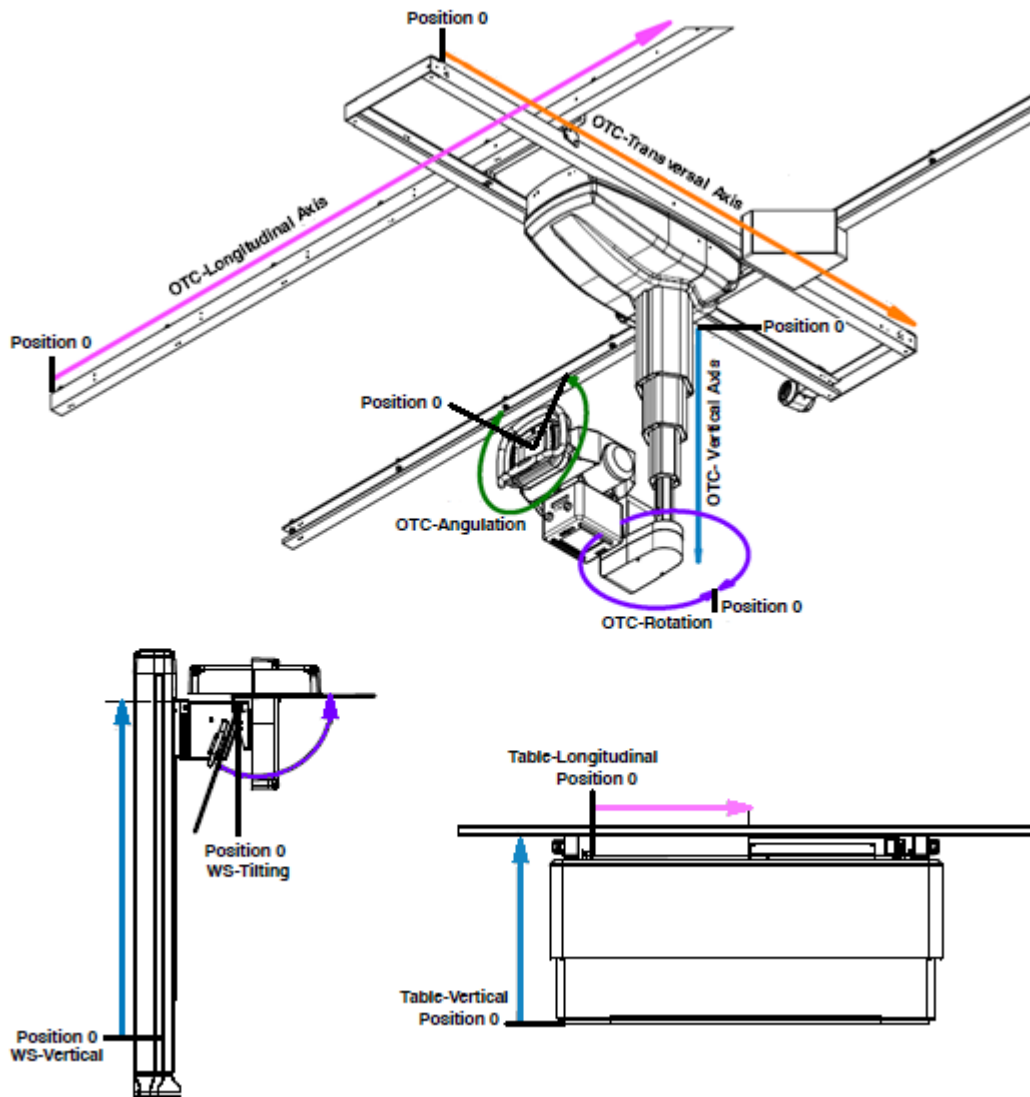
Figure 3.10 Elements found in the X-ray room and the parameters describing their position: (top) X-ray source, (bottom left) wall stand, (bottom right) table

Any combination of these 9 parameters is known as an *autoposition*. In more formal terms, an *autoposition* is defined as the set of parameters or values that describe the exact positioning of the source, table and wall stand elements within the X-ray room.

There is a flash memory located at the ceiling suspension which contains a position database file with defined *autopositions*. New *autopositions* can be created and added one by one to this database using the Suspension Tool (Figure 3.11). The user first creates a new entry (panel 1) to which an ID is automatically assigned. Then, the different parameters are set using the sliders (panel 2) and a description of the *autoposition* has to be provided (panel 3). Finally, the *autoposition* is stored in the database clicking on the save button (panel 4).
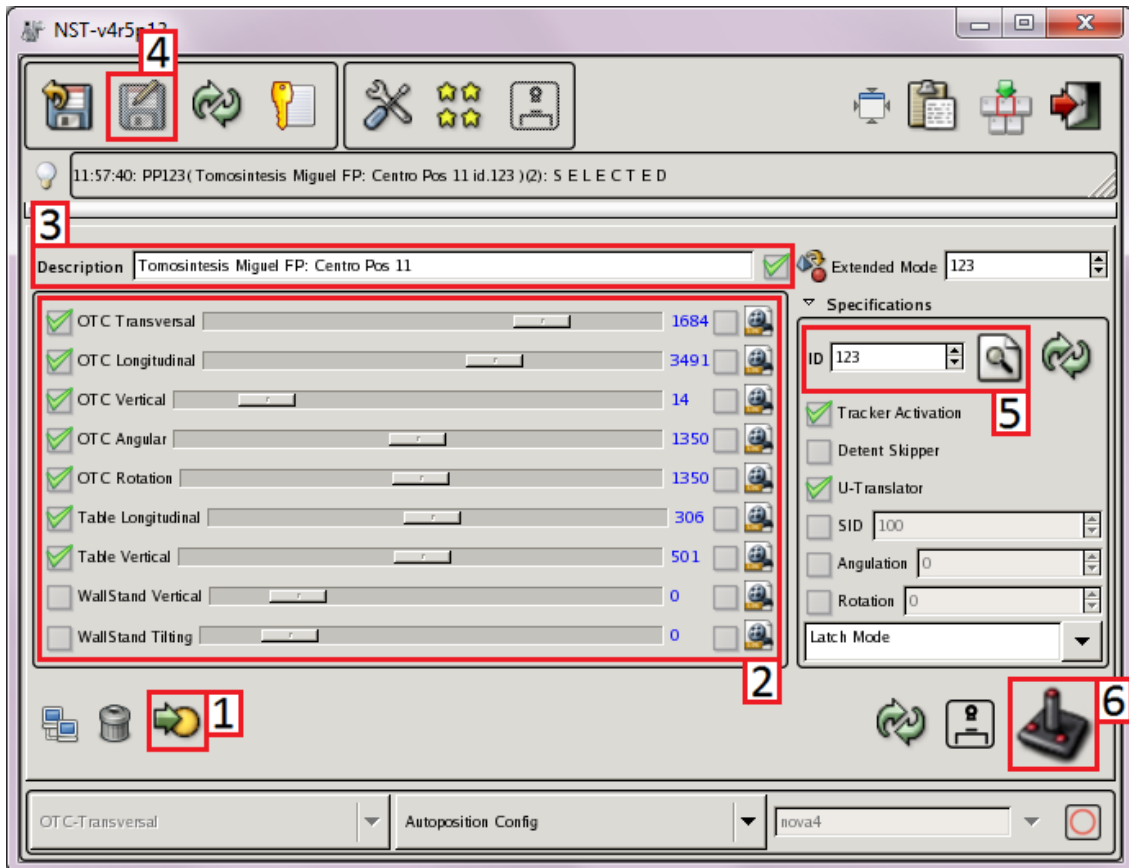
Figure 3.11 Elements of the Suspension Tool used for creating and loading *autopositions*

It must be noted that the creation of new autopositions is slow as it is significantly hampered by the use of sliders.

Stored *autopositions* can be loaded by introducing their corresponding ID (panel 5). Then, the system can be moved to the loaded *autoposition* by clicking on the joystick button (panel 6).

Once the system is at the desired placement, the Generator Interface (Figure 3.12) is used to set the acquisition parameters.
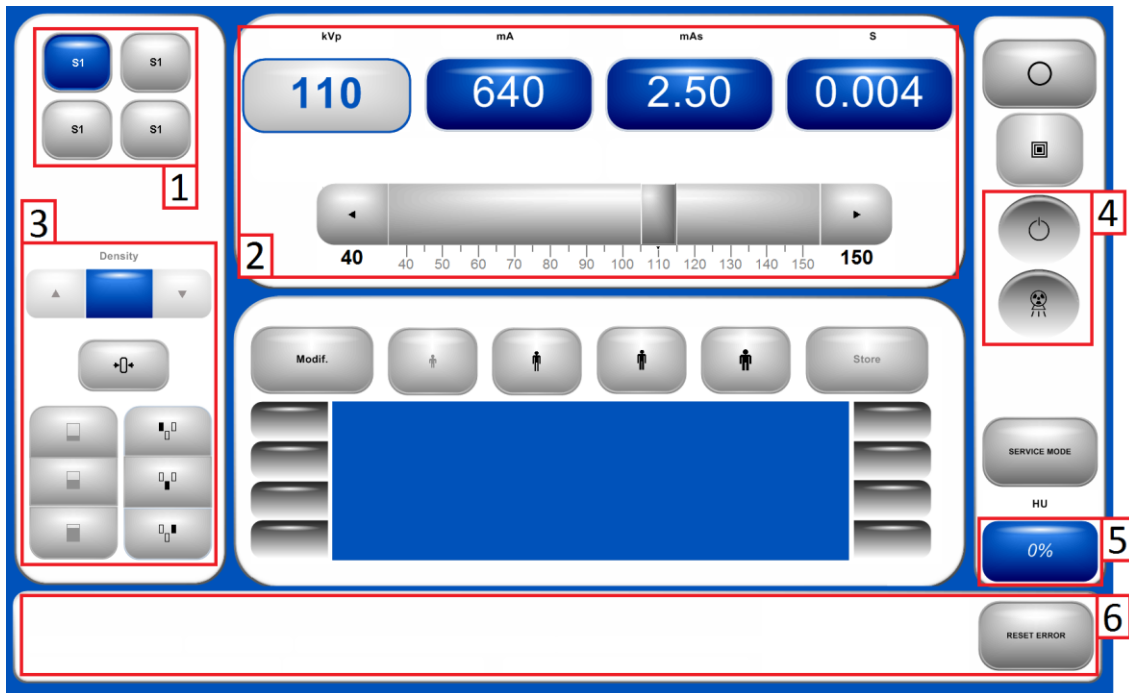
Figure 3.12 Generator Interface

The user first chooses where the projection is to be taken pressing the corresponding *S1* button out of the four available (panel 1). The user may choose: table (top left), wall stand (top right) or free mode (bottom left). The acquisition parameters are set in panel 2. There is a slider whereby the user may adjust the different parameters: voltage, current and time. The user may activate any of the three available ionization cameras (panel 3). These cameras will stop radiation emission once a given radiation exposure has been detected.

The projection is then taken by pressing the hand-switch (Figure 3.13). While the projection is taken, several indicators light up in the Generator Interface indicating when the source is ready to shoot and when it is shooting (panel 4 of Figure 3.12). While shooting, the source becomes hotter. This heating is described as a percentage in panel 6 of Figure 3.12.
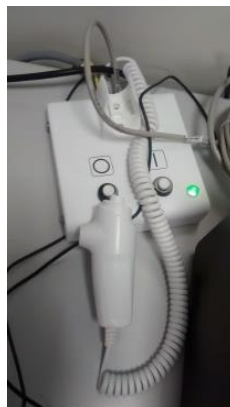
Figure 3.13 Hand-switch

At the bottom of the interface (panel 6 of Figure 3.12), error messages are displayed informing the user of a problem that prevented the source from shooting. For instance, it will display the message *DOOR OPEN* if the user has not closed the door to the X-ray room. The program will not allow making any acquisitions until the user clicks on the *Reset Error* button.

Image Detection

In the NOVA FA system, images are acquired using a Perkin Elmer XRPad 4336 flat panel detector with a pixel size of 100 µm and a matrix size of 4320×3556 pixels. The obtained images are raw data that have to be preprocessed.

Apart from the raw image, two different images are needed for the correction. These are the flood image and the dark image. The dark image represents the signal measured by the detector when there are no incident X-ray photons. This dark image accounts for the dark current or offset of the detector. The flood image is an image obtained in the same conditions as the image to be corrected but without the object. It accounts for the sensitivity difference between detector elements.

The corrected image C is found by modifying the raw projection R using the dark D and flood F images as described by Eq. 3.4:

$$C = \frac{R - D}{F - D}$$

<div align="right">3.4</div>

Dark image does not depend on the intensity of the radiation. Therefore, only a single dark image is acquired per protocol. However, one flood image is required per projection since the intensity of the X-rays reaching the detector is different for each projection.

Along with these differences in gain and offset, the detector may also present malfunctioning pixels. Defective pixels may give no signal (dead pixels), always give the same signal (stuck pixels) or start acting up after long exposures (hot pixels). These pixels can be easily located by performing several acquisitions. Once located, it is possible to correct them by substituting their value by the average signal of the pixels surrounding them.

This whole correcting procedure is known as preprocessing. In order to conduct this preprocessing, a preprocessing tool implemented in Matlab is used. The interface of this tool is shown in Figure 3.14.
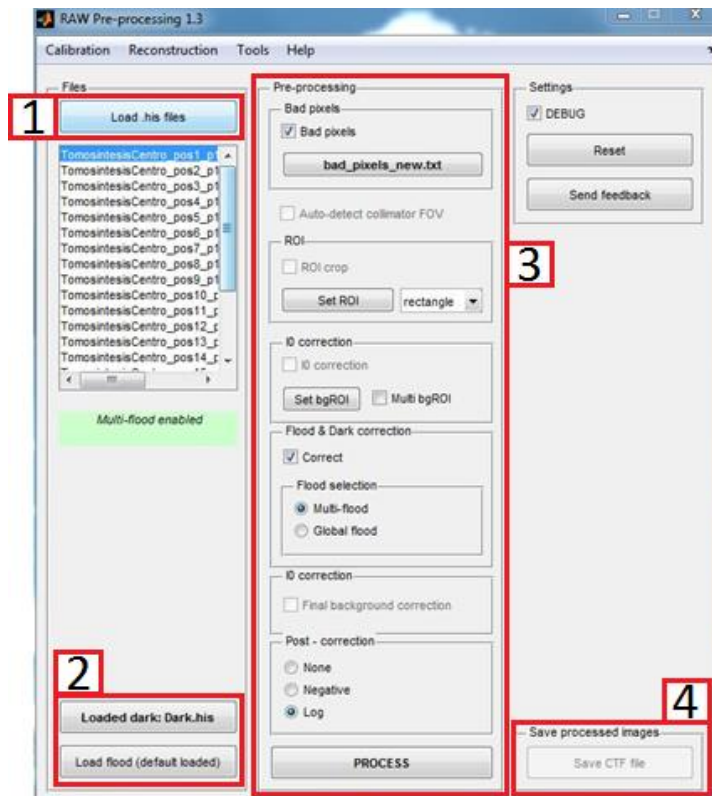
Figure 3.14 Graphical user interface for the preprocessing tool

First, the user loads the set of images to be corrected using the *Load .his files* button (panel 1). If a flood image for each projection is available, the user must load them with the projections. Alternatively, the user can load a single flood to correct the whole set using the *Load flood* button (panel 2). In this same panel, the user can load the dark image. If more than one dark image is loaded, the program will use the mean image for the dark correction.

Once the workflow has been decided, the preprocessing of the images is started pressing the *PROCESS* button at the bottom of panel 3. Once the preprocessing is done, the user can store the corrected images using the *Save CTF file* (panel 4). The program generates two files: a *ctf* file containing the set of corrected images and an *act* file containing the size of the images and the parameters used to acquire them (voltage, current, etc.).

An example of a raw projection and a preprocessed projection is shown in Figure 3.15.
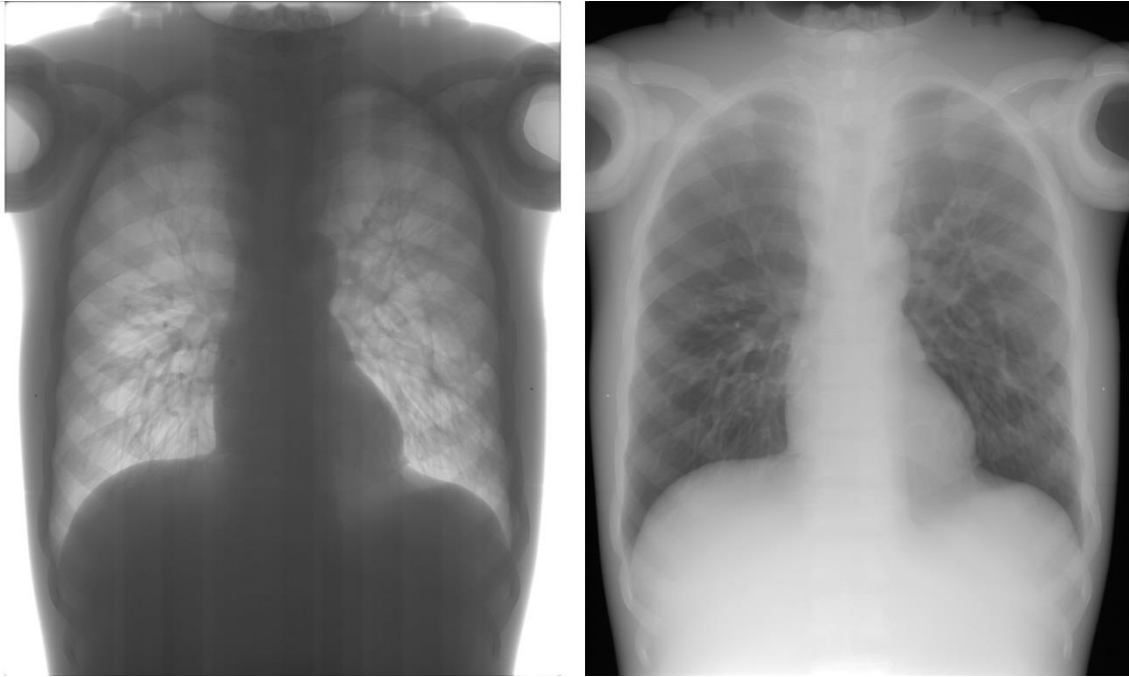
Figure 3.15 (Left) Raw projection of thorax phantom taken from behind
(Right) Projection after preprocessing

3.2.2 Automatization of the Position Database Update

Originally, the incorporation of new protocols could only be done manually using the Suspension Tool to create and store each new *autoposition* as explained in section 3.2.1. This approach, however, is too slow for the incorporation of protocols formed by a large number of positions. The amount of positions that make up tomosynthesis protocols ranges from 20 to 70, and just the creation of 21 *autopositions* can take up to 45 min.

A more automatized workflow was established during this thesis. In this new workflow, the user downloads the position database file from the flash memory of the NOVA FA system using the Putty program through the SSH protocol. The simulation tool explained in section 3.1 then automatically adds the whole set of new positions directly to this file. The updated database then has to be uploaded back to the system. A comparison of both workflows is shown in Figure 3.16.
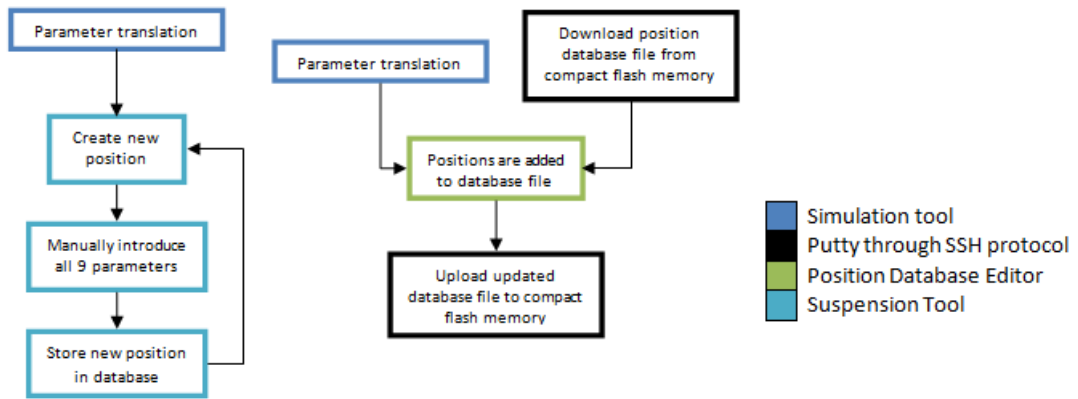
Figure 3.16 (Left) Manual workflow (Right) Proposed automatic workflow

In order to make this workflow possible, the student first saw how information was stored in the position database file and then created a Position Database Editor that could be implemented into the simulation tool described in section 3.1 so as to allow the writing of new *autopositions* by the simulator directly on the database file. The incorporation of the editor to the simulation tool is shown in Figure 3.17.
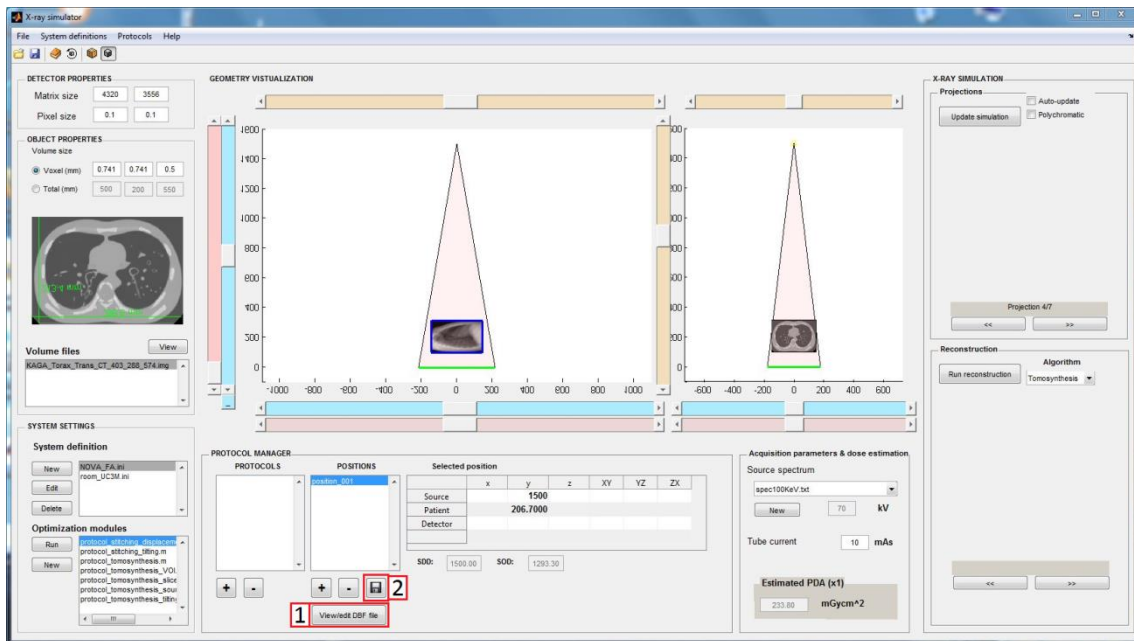
Figure 3.17 Implementation of the DBF editor into the simulation tool

The user can save positions created by the simulation tool in the Position Database file using the save icon (panel 2). The simulation tool first translates the positions into the system of coordinates used by the X-ray room and then the Position Database Editor writes the *autopositions* in the correct format in the database file.

To translate the positions, the position database file was analysed seeing that each *autoposition* is defined by 41 parameters. It is not obvious to identify which elements

40

correspond to what parameter in the database since the name assigned to each parameter is really ambiguous. Using different parameter combinations at the Suspension Tool, it was possible to identify the 11 parameters. These parameters correspond to: *autoposition* ID, *autoposition* description and 9 values corresponding to the position of the X-ray room elements (source, table and wall stand). However, these are enough for the creation of new *autopositions*, as the other could be assigned default values. Nevertheless, the editor allows the user to edit the unidentified values as well.

Additionally, the Position Database file can be seen and manually edited using the *View/edit DBF file* button (panel 1). Clicking on this button opens the Position Database Editor (Figure 3.18).
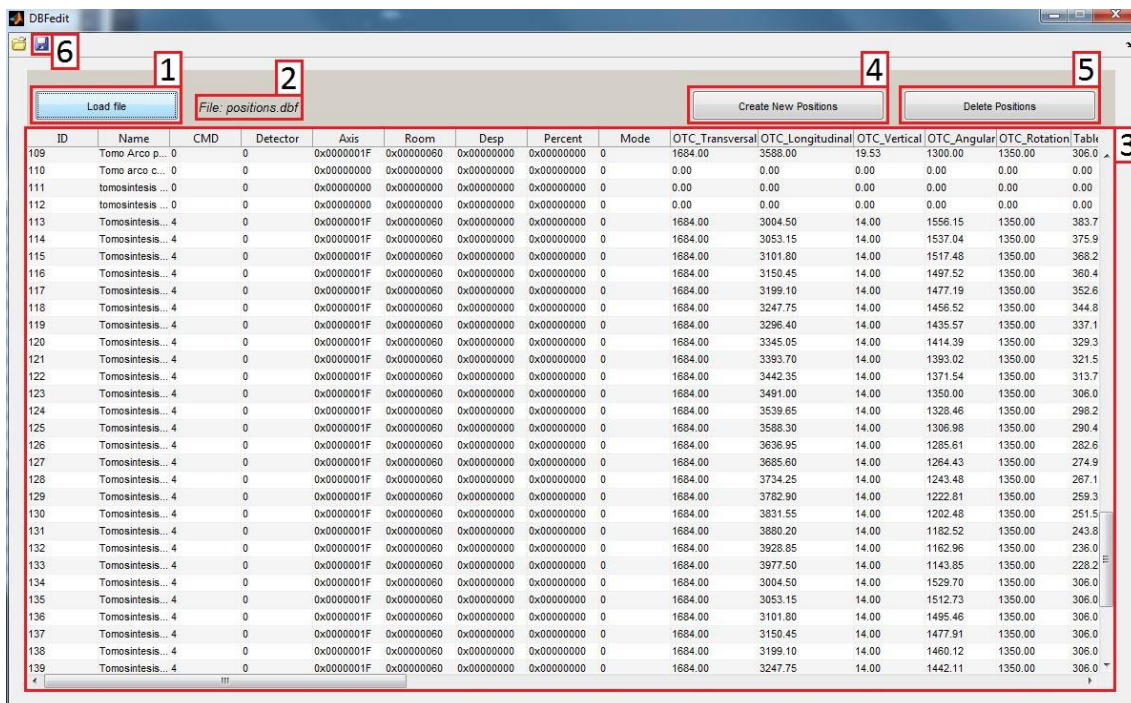
Figure 3.18 Graphical interface of the DBF editor

This program, coded in Matlab, initially displays a blank table and a *Load File* button (panel 1). Using this button, the user can open the *autoposition* database. The program will then display the name of the loaded file (panel 2) and fill out the table with the data contained in the file (panel 3).

Once the file is loaded, two buttons appear: *Create New Positions* (panel 4) and *Delete Positions* (panel 5). The former button opens a window asking for the number of entries to be created and a description shared by them. These new positions are then added to the bottom of the table and the user can manually edit them. The latter button will cause the program to

ask the user for the ID or range of IDs of the *autopositions* to be deleted. Alternatively, the user can highlight the IDs of the *autopositions* to delete and then click on the *Delete Positions* button.

Finally, changes made to the file can be saved using the save icon (panel 6).

The user could then use this editor instead of the Suspension Tool to manually create new *autopositions*. As previously explained, the editor was implemented into the simulation tool allowing it to write new *autopositions* directly in the *autoposition* database (Figure 3.17).

3.2.3 Reconstruction Tool

Following the acquisition in a tomosynthesis protocol, the projections acquired can be used to reconstruct the volume imaged. As explained in the introduction (Section 1.3.3), the Shift-and-Add algorithm is based on shifting each projection obtained a specific amount and then add them all up to bring a given slice into focus. The shifting that must be applied to each projection i in order to reconstruct a slice at a height z is given by Eq. 3.5.

$$shift = x_i - b_i = \left(\frac{z}{D-z} - \frac{z_f}{D-z_f} \right) \cdot a_i \qquad \textbf{3. 5}$$
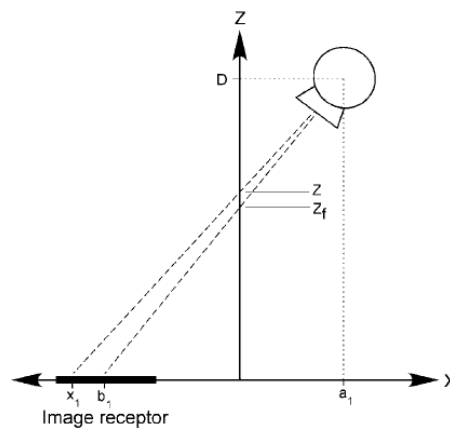
Figure 3.19 Geometry of Shift-and-Add algorithm. Source: [16]

In order to make a Reconstruction Tool, a Matlab function was first created which performed the Shift-and-Add algorithm. For each slice, this function first finds its height z. After that, using the formula given by Eq. 3.5, it finds the shifting that must be applied to each projection. The shifting is then applied to each projection using the *circshift* Matlab function. Finally, the shifted projections are added.

Once this function was made, the interface of the Reconstruction Tool was coded using Matlab. This interface is shown in Figure 3.20.
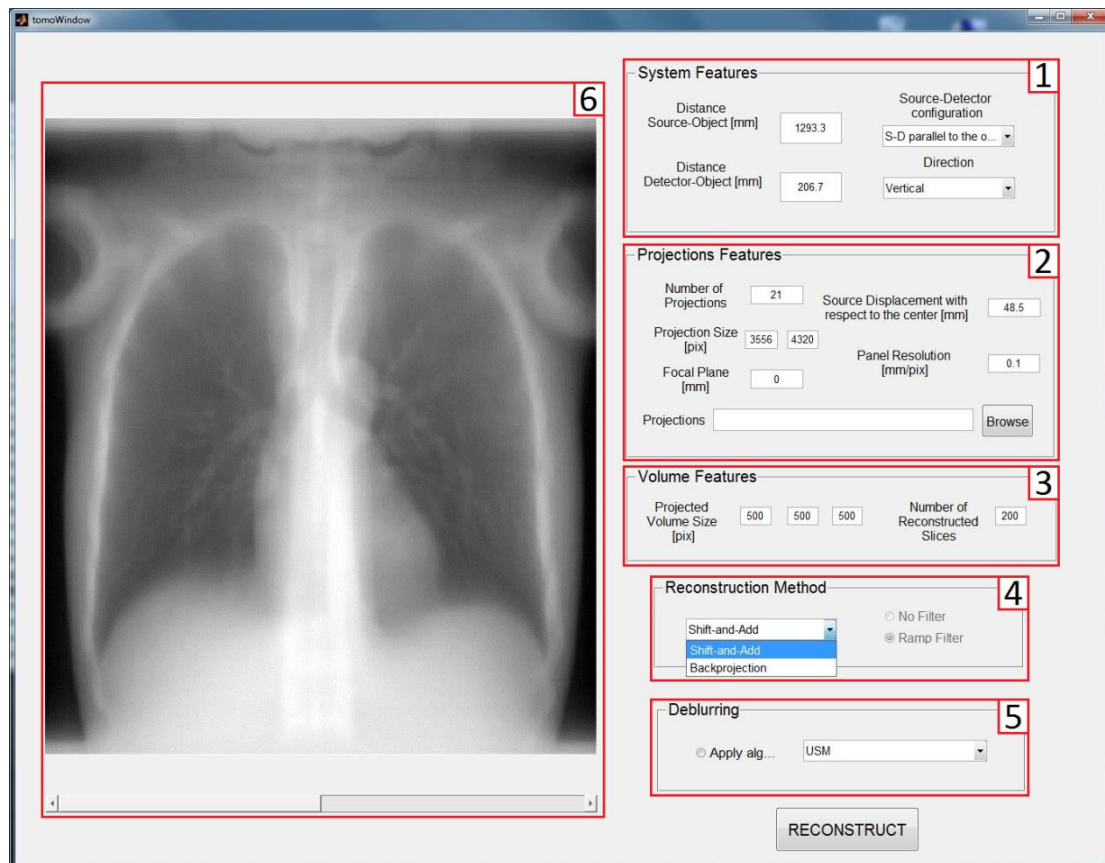
Figure 3.20 Graphical user interface for the reconstruction tool

The interface is composed of five different panels. In the *System Features* panel (panel 1), the user must describe the geometric characteristics of the tomosynthesis protocol used. The proper description of the geometry is paramount, as the implementation of the reconstruction algorithm depends on the source-detector configuration. The tool allows choosing two different configurations: *S-D parallel to the object* and *S arc/D static*. The former refers to the detector and source moving in parallel planes to the body in opposite directions. On the other hand, the latter refers to the source moving in an arc while the detector remains static. Out of these two options, however, only the reconstruction algorithm for the first one, i.e. *S-D parallel to the object*, had been implemented as of the writing of this thesis.

Other parameters to introduce in the *System Features* panel are: the distance from the source and from the detector to the middle of the body (*Distance Source-Object* and *Distance Detector-Object*, respectively) and the direction along which the source was moving during the acquisition process with respect to the images (*Direction*).

In the *Projection Features* panel (panel 2), in order to properly load the projections acquired, certain features have to be specified. These are:

· Number of projections: the amount of projections acquired, usually an odd number.

· Source displacement: the displacement in millimetres of the source between projections.

· Projection size: width and height of each projection in pixels; correspondingly, the size of the detector.

· Detector resolution: pixel size of the detector.

· Projections: using the *Browse* option, the directory containing the projections is introduced; only to be used once the other parameters have been filled out.

The projections are then loaded and displayed in the left hand side of the interface (panel 6).

The *Volume Features* panel (panel 3) must be filled out with the size in pixels of the volume to be reconstructed (*Projected Volume Size*) and the number of slices to be reconstructed (*Number of Reconstructed Slices*). The number of reconstructed slices, therefore, may not be larger than the size of the volume in the *z* direction.

The *Reconstruction Method* panel (panel 4) is used to specify which reconstruction algorithm the user wants to apply. The interface was made in a modular way so that more reconstruction algorithms can be implemented. Therefore, aside from the Shift-and-Add function created in this thesis, a previously available Backprojection reconstruction function was added.

Finally, a deblurring algorithm may be applied so as to improve the quality of the reconstruction. The user can choose whether to apply a deblurring algorithm in the *Deblurring* panel (panel 5) and, if so, which algorithm to use. As of the writing of this thesis, this panel had not been fully functional.

Once everything is set, the user may initiate the reconstruction clicking on the *RECONSTRUCT* button. The interface then displays the result in panel 6.

3.4 Complete Workflow

Once all the necessary tools were ready, it was possible to establish the workflow for the implementation of tomosynthesis acquisition protocols into the radiology system. The complete workflow is displayed in Figure 3.21.
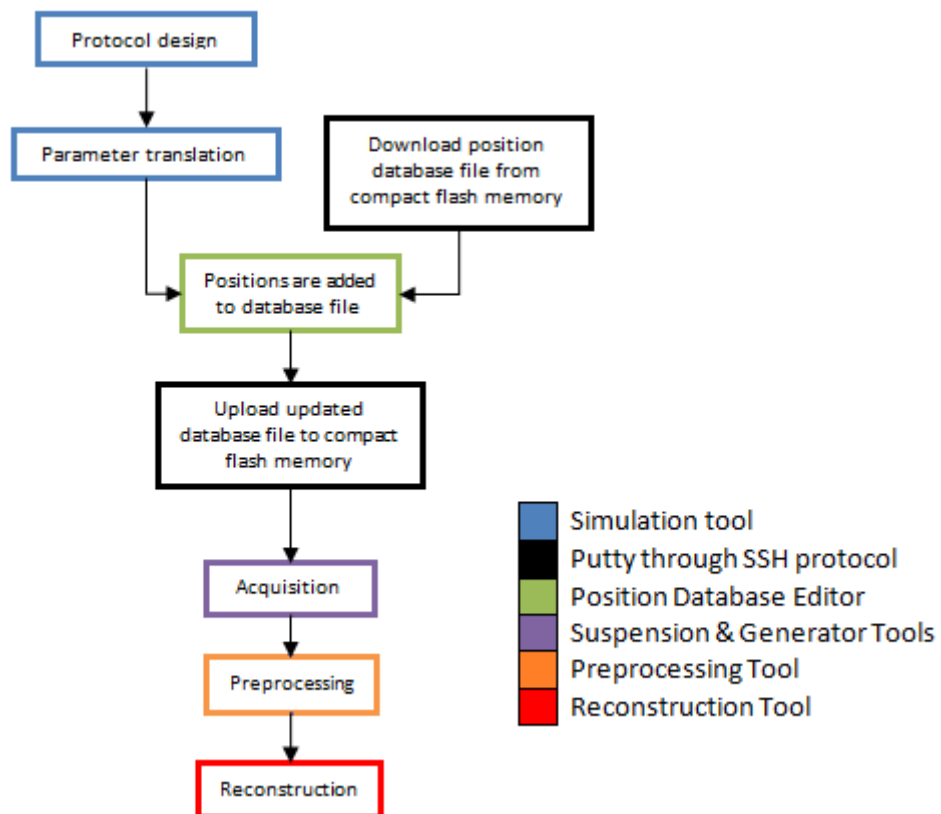
Figure 3.21 Proposed workflow for the implementation of tomosynthesis protocols to the NOVA FA radiology system

The user first designs the protocol by means of the tomosynthesis module that has been incorporated to the simulation tool. Once the design is complete, the user must download the current *autoposition* database file from the compact flash memory at the ceiling suspension of the NOVA FA system. The simulation tool then translates the source-detector positions into the corresponding *autopositions* and then calls the DBF Editor to automatically add them to the database file. The updated database file is then re-uploaded using the Putty program through the SSH protocol.

The user then proceeds to the acquisition. The acquisition parameters are first set using the Generator Interface. Then, the user uses the Suspension Interface to manually load each *autoposition* and move the system, acquiring a projection from each *autoposition*. After acquiring the projections, the user must remove the object to acquire a flood image from each *autoposition* and a dark image for preprocessing.

Once every projection has been obtained, each image must be processed using the preprocessing tool. This preprocessing step is then followed by a reconstruction step using the developed Reconstruction Tool.

4 Evaluation

Two different evaluations were conducted in order to analyse the feasibility of the proposed workflow for the implementation of tomosynthesis to the NOVA FA system.

First, a geometrical evaluation was conducted. This was performed using a simple phantom in order to see whether the projections given by the simulation tool correspond to what is obtained in the real NOVA FA system. A second study was conducted to evaluate the whole workflow. This involved the design of a simple tomosynthesis acquisition protocol to be incorporated to the system. The phantom used in this case was the thorax of a whole body phantom PBU-50, manufactured by Kyoto Kagatu.

The following sections contain a detailed description of the two evaluations.

4.1 Geometric Evaluation

To conduct the geometric evaluation, a phantom made of 15 radiopaque markers with a 2.3 mm diameter supported by a polystyrene cube was used. One of the markers and the complete phantom are shown in Figure 4.1.
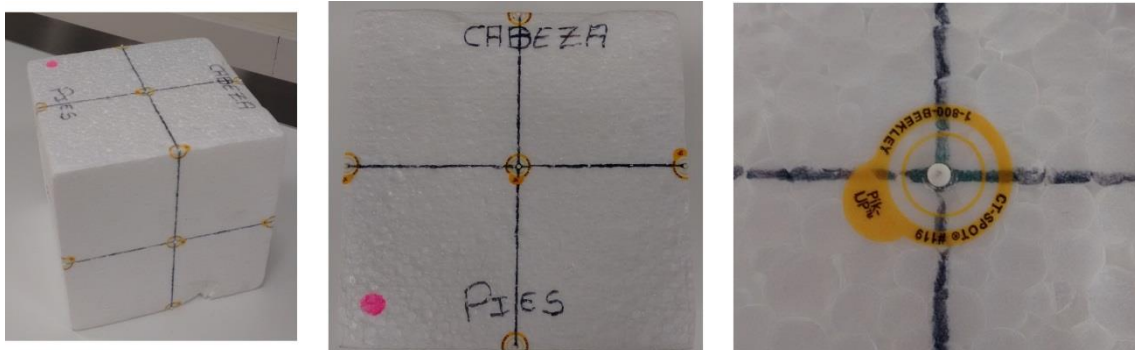
Figure 4.1 (Left) Phantom used in this evaluation
(Middle) Top view of the phantom
(Right) Zoom-in to one of the markers

This evaluation was conducted following the workflow shown in Figure 4.2. First, a CT scan of the phantom was acquired. A simple acquisition protocol of three projections was designed using the simulation tool described in section 3.1 (Figure 4.3). Then, the CT scan was used to obtain three simulated projections at these positions. The used source-detector positions were then translated and added to the position database file. The updated database was uploaded to the system and the corresponding projections were acquired. Finally, both sets of images were compared using a Matlab code implemented for this purpose.
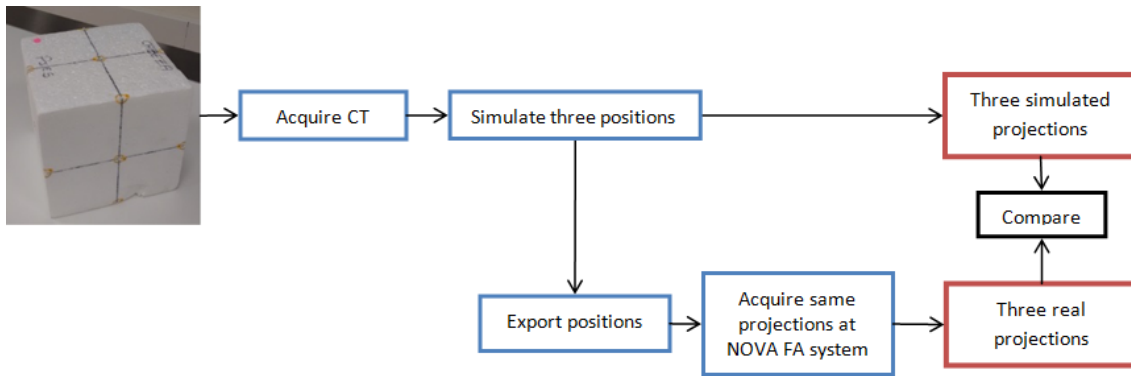
Figure 4.2 Workflow followed for the geometric evaluation
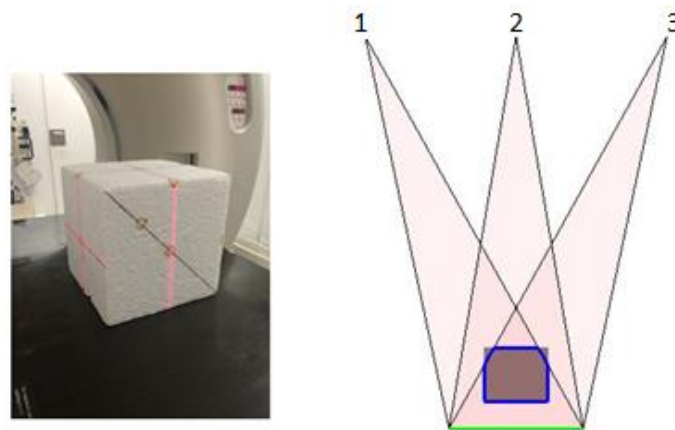
Figure 4.3 (Left) Phantom in the CT
(Right) Diagram showing projections of the phantom obtained

The real and simulated versions of projection 2 are shown in Figure 4.4. In order to properly compare the real set of images with the simulated set, the markers had first to be extracted. To this aim, threshold segmentation was applied to both sets using the software ImageJ.
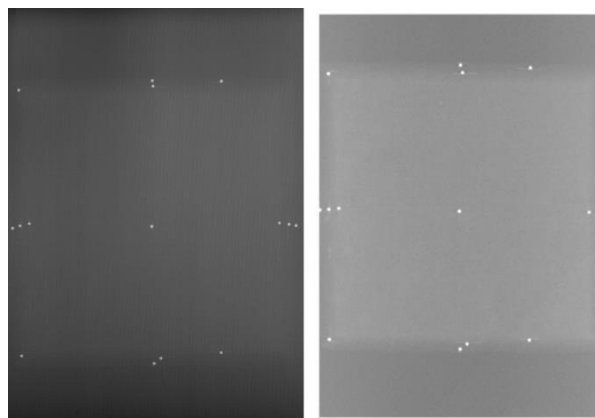
Figure 4.4 Real (left) and simulated (right) versions of the second projection

The images displaying the segmented markers for projection 2 are shown in Figure 4.5.

A Matlab code was then made to compare the segmented sets. First, using the Matlab function *bwlabel*, each marker was labelled. As there were 15 markers, this means that they were assigned a number from 1 to 15. Once labelling was completed, each marker was reduced to a single point: its centre of mass. The coordinates of each centre of mass is shown in Eq. 4.1.

$$X_{cm} = \frac{\sum_i x_i}{N} \quad Y_{cm} = \frac{\sum_i y_i}{N}$$

4.1

Figure 4.6 shows the real and simulated sets of markers of projection 2 in a single image as well as the corresponding label assigned to each marker.

It can be seen that both sets of markers are misaligned, which is likely due to the difference in position of the phantom in the real system. This is because the CT and the NOVA FA system are very different and it is very difficult to position the phantom in the exact same way in two

completely different pieces of equipment. Therefore, both sets of images were then registered. This involved finding the rotation $\boldsymbol{R}$ and translation $\boldsymbol{T}$ that best aligned the real set of markers r to the simulated set s. Applying the found rotation $\boldsymbol{R}$ and translation $\boldsymbol{T}$ to the real set r converted it to the registered set $\hat{r}$, as can be seen in Eq. 4.2.

$$\hat{r} = \boldsymbol{R}r + \boldsymbol{T} \qquad \text{4.2}$$

Figure 4.7 shows both sets of markers of projection 2 after registration.
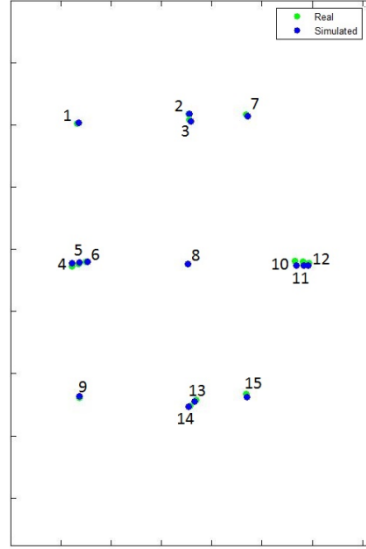
Figure 4.7 Figure showing real and simulated sets of markers of the second projection in a single image after registration

The fiducial registration error FRE was then computed according to Eq. 4.3.

$$FRE^2 = \frac{1}{N} \cdot \sum_i |\boldsymbol{R}r_i + \boldsymbol{T} - s_i|^2 \qquad \text{4.3}$$

The FRE was found to be 1.8 mm which implies that the simulator adequately represents what the real system would acquire. The differences noted earlier could be attributed to small deviations with respect to the placement of the phantom in the real system. That is, while the simulator perfectly aligns the phantom with the source, it is not as easy to manually do so at the X-ray room.

4.2 Evaluation of the Complete Proposed Workflow

This evaluation was conducted using the thorax of a PBU-50 Kyoto Kagatu whole body phantom (Figure 4.8). A CT scan of this phantom was acquired with a Toshiba Aquilion/LB (512x512x1645 voxels, 0.931x0.931x0.5 mm voxel size) to use it for the design of the tomosynthesis protocol.

Figure 4.8 (Left) Whole PBU-50 anthropomorphic phantom, (middle) thorax of PBU-50 phantom and (right) axial, coronal and sagittal views of the CT volume

A simple tomosynthesis acquisition protocol was designed using the simulation tool described in section 3.1, which was then implemented in the NOVA FA system. After that, projections of the PBU-50 thorax were obtained and then used by the Reconstruction Tool described in section 3.2.3 to reconstruct the volume.

4.2.1 Tomosynthesis Acquisition Protocol Design

The design of the tomosynthesis acquisition protocol was based on several implementations described in the literature. Several authors tried to find the best acquisition parameters for different structures of interest [17, 19, 36, 38-40]. An example is presented in Table 4.1.

Anatomic Site	Preferred Parameters	
	Sweep Angle (degrees)	No. of Projections
Abdomen	20	25
Chest	30	60
Hip joint	40	60
Cervical spine	40	60

Table 4.1 Preferred parameters for digital tomosynthesis at various anatomic sites found by Machida *et al* [17]

The implementation extracted from the literature [17] is shown in Figure 4.9a. The patient stands in front of the wall stand in posteroanterior (PA) position (with their back to the source) and 21 projections equally spaced along 973 mm were taken. Thorax projections are acquired using the wall stand with the source at 1800 mm from the detector.

The replication of this implementation would imply finding some support to hold the thorax phantom in place when acquiring using the wall stand. For the sake of simplicity, tomosynthesis was implemented using the table instead (Figure 4.10). However, at the table, the source can only be positioned as far as 1500 mm from the detector (Figure 4.9b).
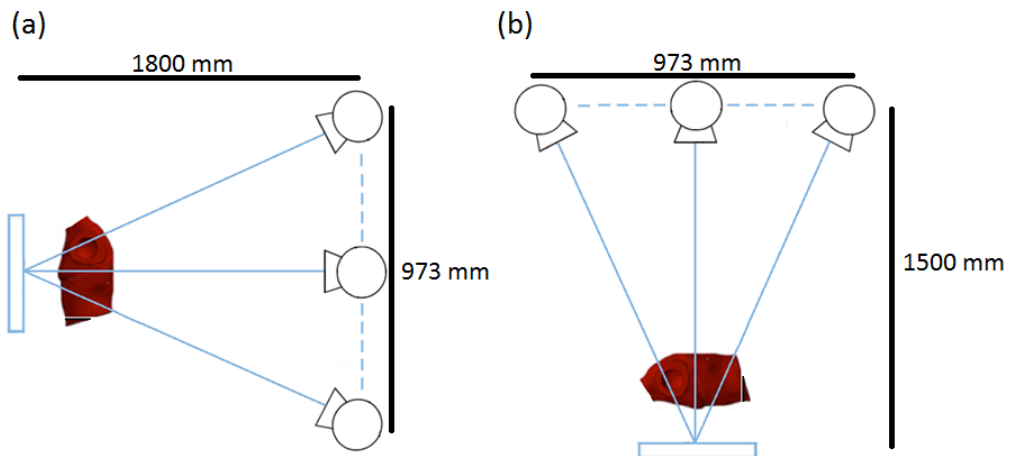
Figure 4.9 (a) Tomosynthesis implementation extracted from literature (b) Proposed tomosynthesis implementation

Figure 4.10 Placing the phantom at the wall stand (left) and at the table (right)

Therefore, the first step was to see if changing the source-detector distance would have a significant effect on the projections obtained.

Using the simulation tool described in Section 3.1, one single projection was obtained at both distances: 1500 mm and 1800 mm, which correspond to acquisitions performed at the table and at the wall stand, respectively.

One of the differences to be expected due to the change in distance was in magnification. As described in the introduction (Section 1.2), magnification depends on the distances between the source and the detector (source-detector distance) and between the source and the patient (source-object distance).

With regards to this particular case, both the source-detector and source-object distances change. The magnifications at 1800 mm and at 1500 mm for the centre slice of the patient are given by Eq. 4.4 and 4.5:

$$M_{1800} = \frac{1800}{1800 - 206.7} = 1.13 \qquad \text{4.4}$$

$$M_{1500} = \frac{1500}{1500 - 206.7} = 1.16 \qquad \text{4.5}$$

The projected size of thorax structures was, therefore, expected to be slightly larger at 1500 mm than at 1800 mm. This was checked by measuring the size of the lungs at projections at both distances. Taking into account that the pixel size of the detector is 0.1 mm, the size of the left lung was 237.6 mm at 1500 mm and 232.2 mm at 1800 mm (Figure 4.11).
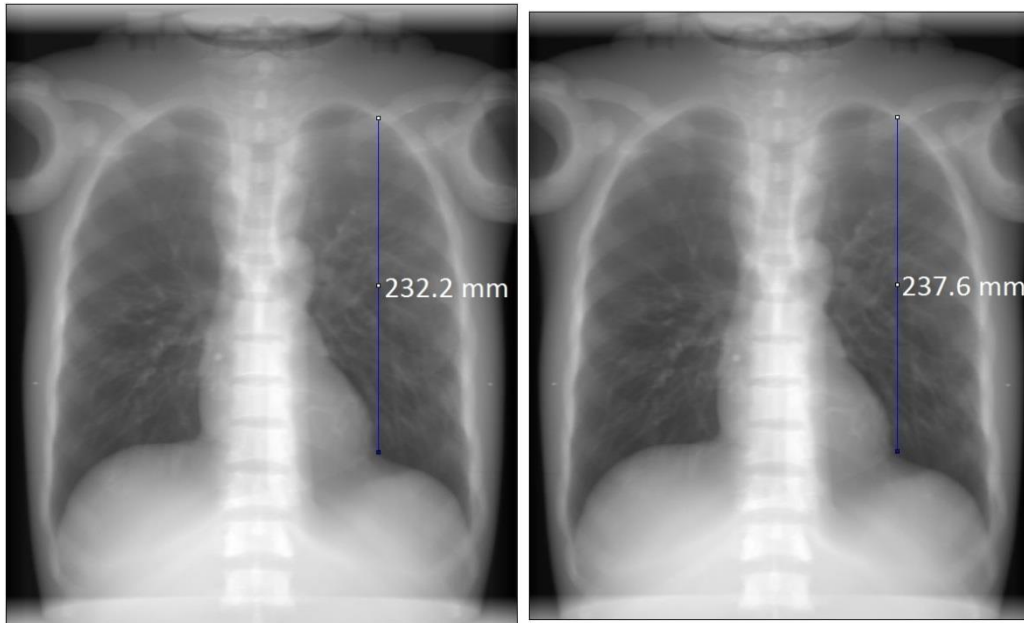
Figure 4.11 Simulated projections taken from behind at 1800 mm (left) and at 1500 mm (right)

Aside from magnification, it was possible for the contrast resolution to have changed due to the change in source-detector distance. To check whether this change had occurred, a profile was taken along the left lung in both acquisitions and compared. Before doing so, however, one of the images had to be resized so that the left lung occupied the same amount of pixels in both acquisitions. The resize factor RF that has to be applied is the ratio between both magnifications (Eq. 4.6).

$$RF = \frac{M_{1800}}{M_{1500}} = \frac{1.13}{1.16} = 0.977 \qquad \text{4.6}$$

Therefore, the 1500 mm image was resized by a factor of 0.977. Doing so resulted in the left lung measuring 2322 pixels in both images.
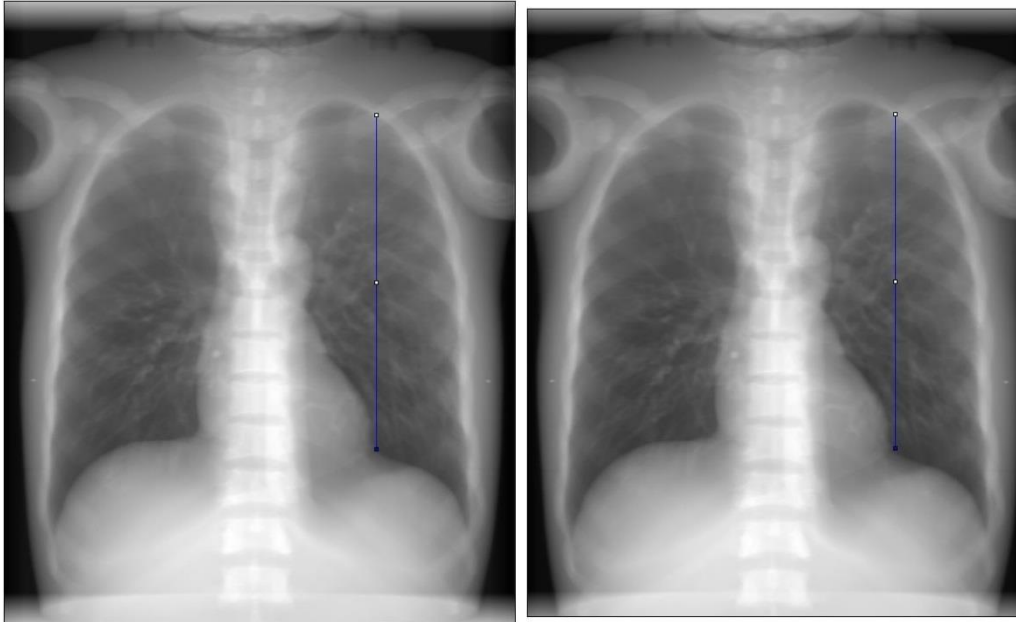
Figure 4.12 (Left) Simulated projection at 1800 mm
(Right) Resized simulated projection at 1500 mm

The profiles were taken along the lines shown in Figure 4.12 and can be seen in Figure 4.13. It can be seen that there was no significant change in the contrast obtained.
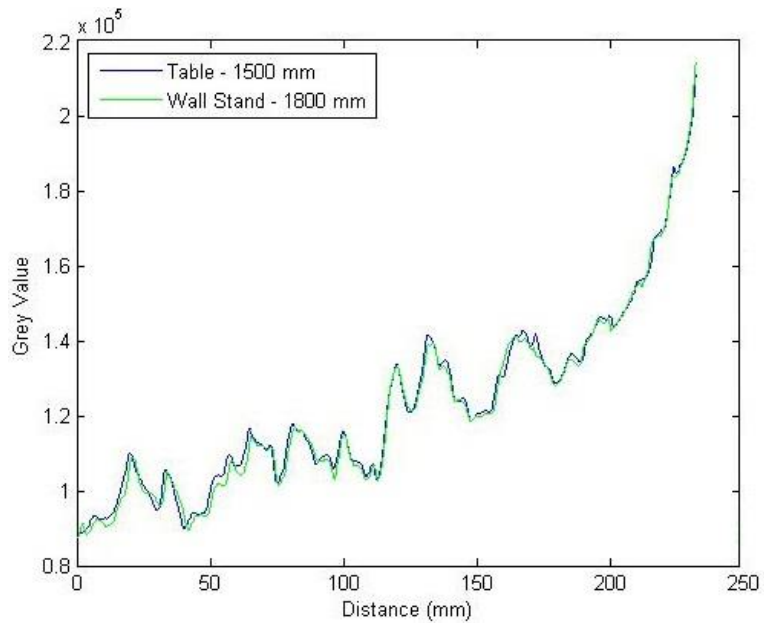
Figure 4.13 Grey value profiles for simulated projections at 1800 mm (green) and at 1500 mm (blue)

Finally, regarding the tomosynthesis protocol (21 projections along 973 mm), due to the different source-detector distance, the slice thickness and the field of view (area where every single projection overlaps) changed (Figure 4.14). The field of view at 1500 mm is slightly more limited; however, the lungs still fit within it. The slice thickness, on the other hand, is improved as it is reduced by 0.62 mm.

Focal plane = -206.70mm
Slice thickness = 3.70 mm

Focal plane = -206.70mm
Slice thickness = 3.08 mm
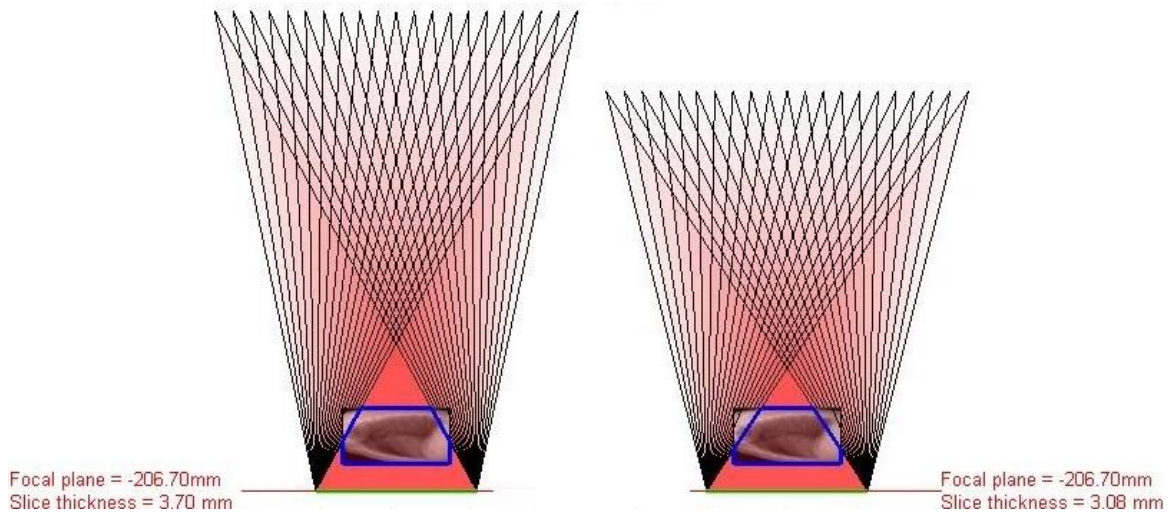
Figure 4.14 (Left) GE tomosynthesis implementation: 1800 mm (wall stand)
(Right) Proposed tomosynthesis implementation: 1500 mm (table)
In blue: part of the volume within the FOV

The design extracted from the literature did not specify where the focal plane is placed. Therefore, the effects of placing the focal plane at two different heights were compared: on the detector and in the middle of the patient.

A schematic representation of the effects of changing the focal plane location can be seen in Figure 4.15. The effect of changing the position of the focal plane is twofold: not only is the field of view affected but the slice thickness changes too. The field of view of any tomosynthesis protocol corresponds to the area where every single projection overlaps. This area changes depending on where the focal plane is placed: a pentagonal field of view is obtained when placing the focal plane in the middle of the phantom; on the other hand, placing the focal plane on the detector results in a triangular field of view. In the first case, the whole thorax phantom fits within the field of view while in the latter both ends of the thorax are left out.
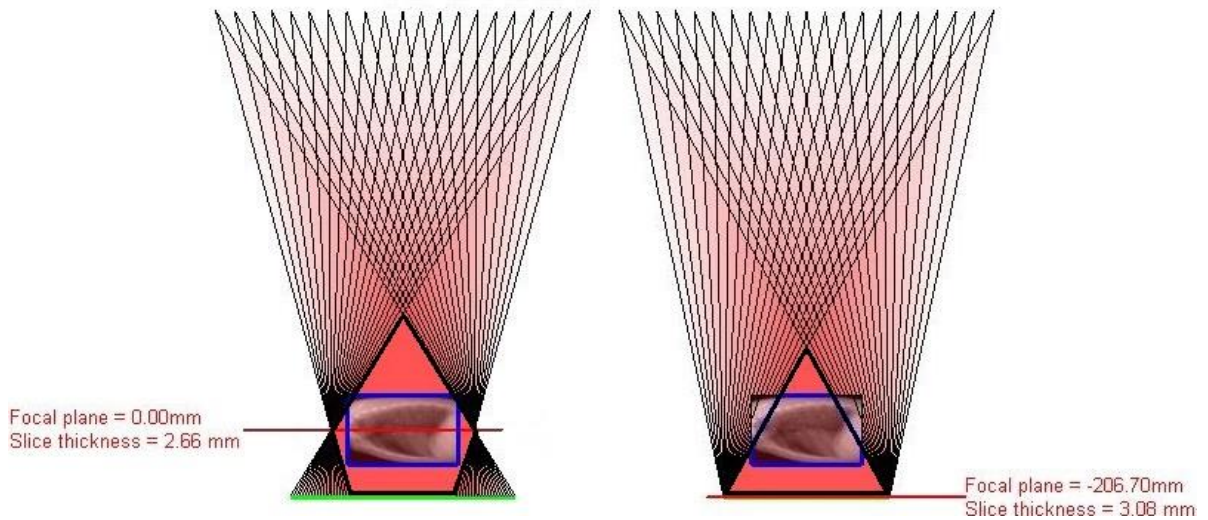
Figure 4.15 Field of view and slice thickness obtained when placing the focal plane in the middle of the patient (left) and on the detector (right)

The difference in the field of view between both configurations can be observed in the projections and in the reconstruction. Figure 4.16 shows that the whole thorax can be seen in all 21 projections when the focal plane is in the middle of the patient. When placing the focal plane on the detector, certain parts of the thorax cannot be seen in some of the projections; e.g. the neck of the phantom cannot be seen in the twenty-first projection.
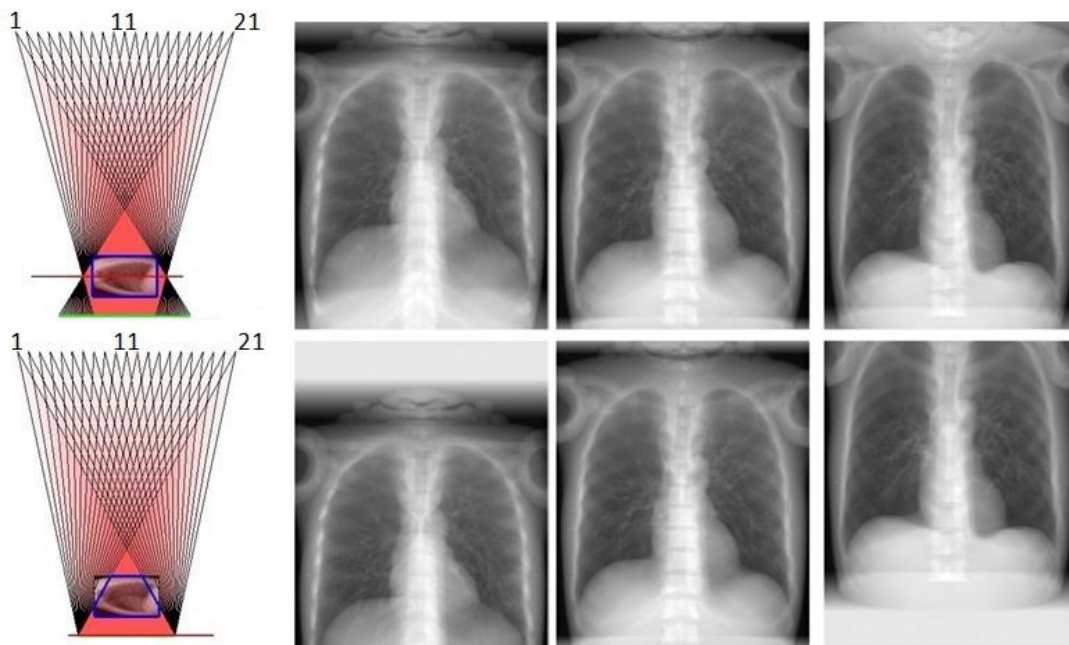
Figure 4.16 Simulated projections 1, 11 and 21 at 1500 mm placing the focal plane in the middle of the patient (top row) and on the detector (bottom row)

With regards to slice thickness, as the focal plane is closer when the focal plane is in the patient, the angle covered by the source is bigger. This implies that this configuration will yield a thinner slice thickness.

Placing the focal plane on the detector has been proven to have a more limited field of view and a thicker slice thickness. However, the lungs are unaffected by these two effects as they still fit within the field of view. Aside from this, placing the focal plane on the detector implies that the detector itself does not move, which makes its implementation that much easier.

The final tomosynthesis protocol design (Figure 4.17) that was to be implemented is the following: the source moves linearly over 973 mm acquiring 21 equally spaced projections at a distance of 1500 mm from the patient, which lies on the table with his back to the source. The detector, on the other hand, does not move as the focal plane is placed on it.

Focal plane = -206.70mm
Slice thickness = 3.08 mm
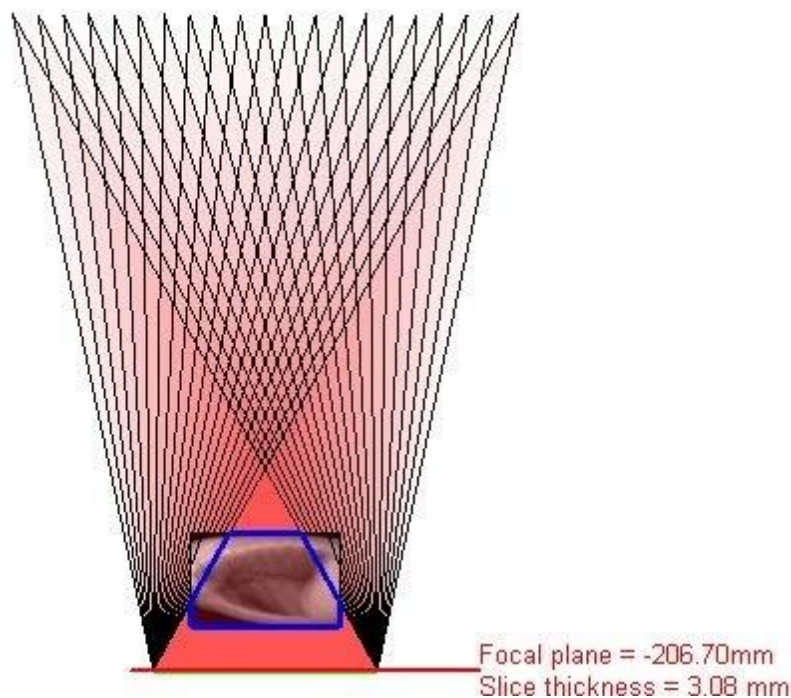
Figure 4.17 Final tomosynthesis protocol design to be implemented

4.2.2 Implementation & Acquisition at the NOVA FA System

The *autopositions* defining the designed protocol were generated by the simulation tool. The position database file was then downloaded from the system and updated with the new positions. This file was then taken to the X-ray room at the *Universidad Carlos III* and uploaded to the compact flash memory of the ceiling suspension. The NOVA FA system positioned in the middle projection with the phantom in PA position is shown in Figure 4.18.
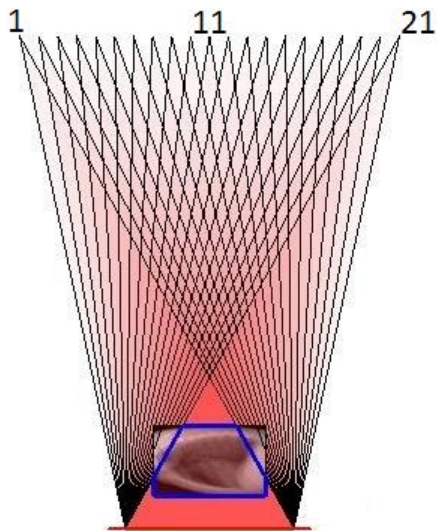
Figure 4.18 (Left) Diagram showing implemented tomosynthesis protocol
(Right) Middle autoposition (number 11) of the tomosynthesis protocol in the X-ray room

The acquisition parameters chosen for this protocol (Figure 4.19) correspond to the ones commonly used for clinical thorax acquisitions.

kVp	mA	mAs	S
110	640	2.50	0.004

40   40   50   60   70   80   90   100   110   120   130   140   150   150
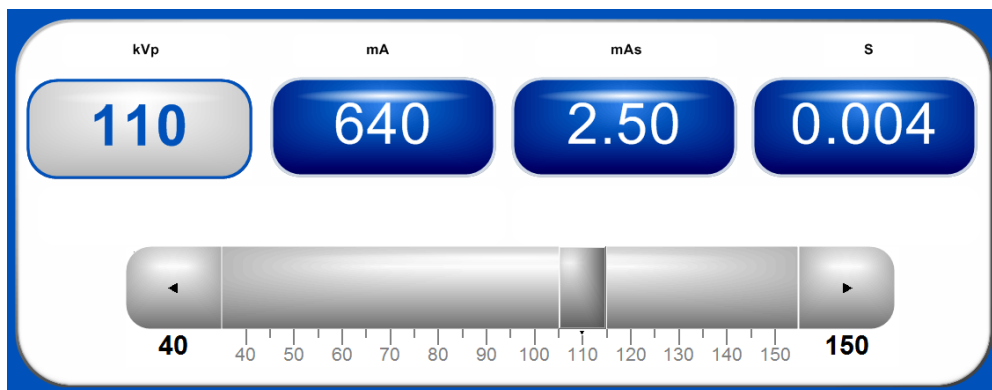
Figure 4.19 Acquisition parameters used in the implemented tomosynthesis protocol

Some of the acquired projections, after preprocessing, are shown in Figure 4.20. The corresponding simulated projections are shown below them. It must be noted that the CT used has the head of the phantom attached. Aside from that, both sets can be seen to be very similar.

57
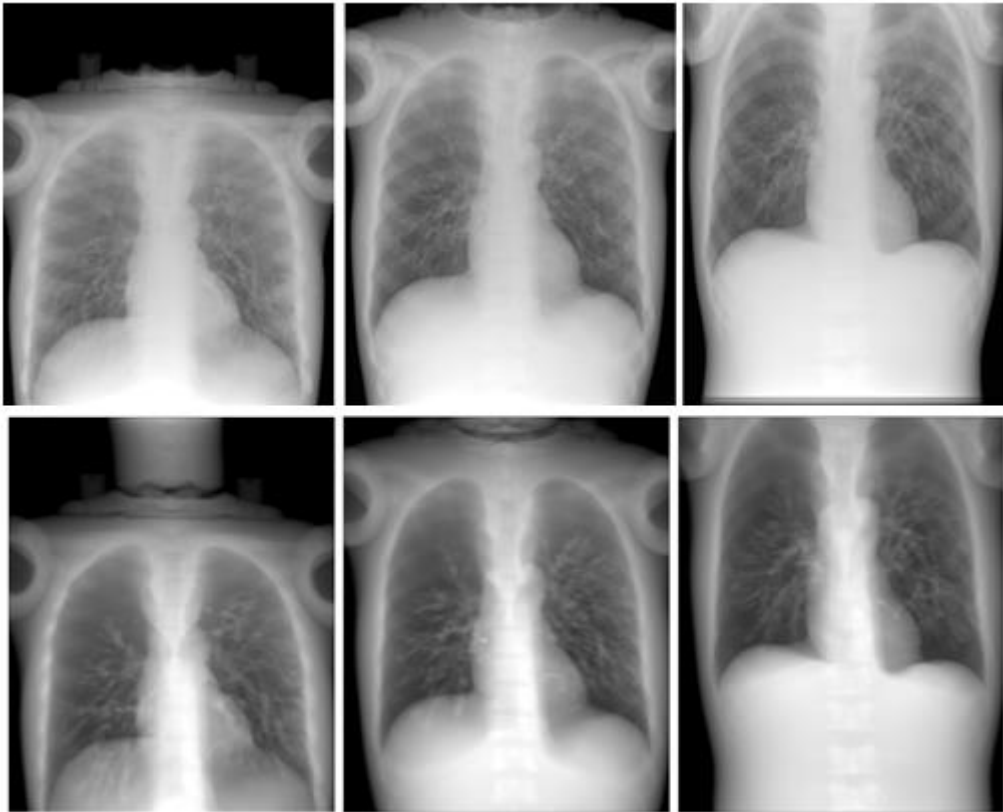
Figure 4.20 (Top row) Acquired projections 1, 11 and 21 belonging to the implemented tomosynthesis protocol (Bottom row) Corresponding simulated projections

Using the preprocessed images, the volume was reconstructed using the Shift-and-Add algorithm. The resulting volume focused at different slices is shown in Figure 4.21.
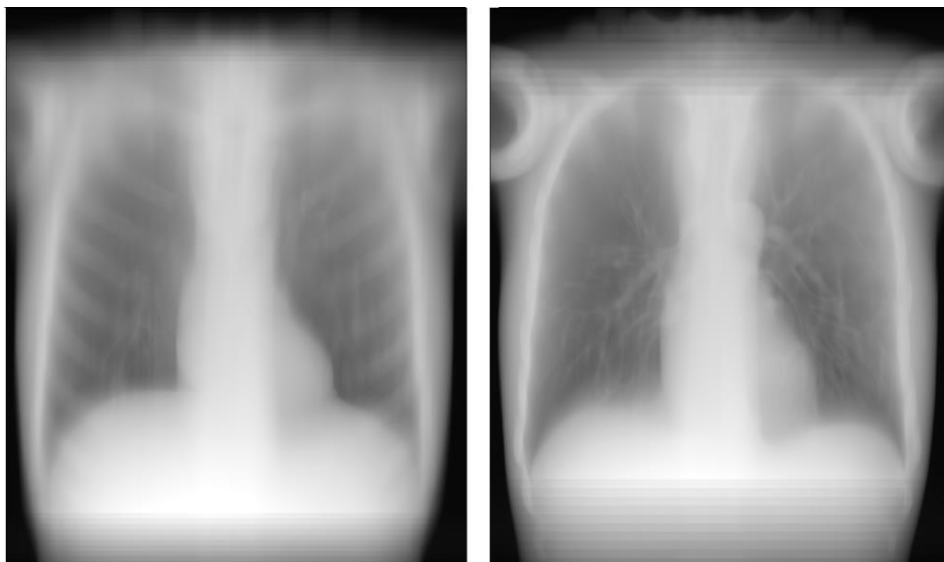
Figure 4.21 Reconstructed volumen using Shift-and-Add (Left) Focused on ribs (Right) Focused on lungs

Finally, the volume was reconstructed using the Backprojection algorithm, both filtered and non-filtered. Examples of reconstructed slices using each method can be seen in Figure 4.22.
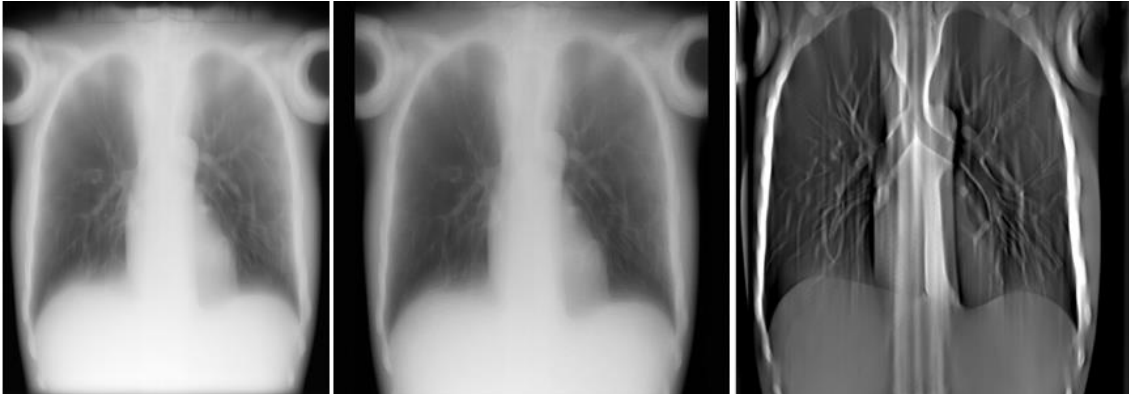
Figure 4.22 Reconstructed volume focused at a slice in the lungs
(Left) Shift-and-Add (Middle) Plain Backprojection (Right) Filtered Backprojection

5 Conclusions & Future Work

5.1 Conclusions

The present thesis has focused on the incorporation of tomosynthesis capabilities to a system originally designed for planar imaging: the NOVA FA digital radiography system. To this aim, a complete workflow, starting from the design of the protocol down to the reconstruction step, including the implementation of the acquisition on the real system, has been established. The work has entailed the tasks described below.

A software tool has been prepared for the design of tomosynthesis acquisition protocols. To this end, a tomosynthesis module has been incorporated to an in-house X-ray protocol simulation tool implemented in Matlab and CUDA. Using this module, tomosynthesis protocols with parallel path geometry can be easily designed by setting some of the following acquisition parameters: number of projections, focal plane placement, slice thickness, maximum source displacement and field of view.

The X-ray room was built specifically for research: everything is manual and all the software is open. This system was designed only for planar radiography and, as a consequence, it is very cumbersome to incorporate a protocol composed of several projections. Therefore, this task was made easier by developing a Matlab tool that allows the translation of each of the source-detector positions corresponding to the tomosynthesis design to the geometrical parameters of the NOVA FA system and their automatic addition to its database. Thanks to this, the time at which protocols are incorporated has been considerably decreased reducing, for instance, the 45 min needed for a 21 position protocol to mere seconds.

To obtain tomography image from the acquired data, a reconstruction tool for tomosynthesis has been developed using Matlab. The user interface allows reconstructing any volume acquired using a tomosynthesis acquisition protocol with parallel path geometry. This tool was developed in a modular way so that new reconstruction algorithms can be easily incorporated, as demonstrated with the incorporation of a Backprojection algorithm, commonly used for CT.

The development of all of these tools allowed setting up the workflow for the incorporation of tomosynthesis protocols to the NOVA FA system. The workflow has been evaluated with two different studies. A geometric evaluation to see the correlation between the simulation tool and the system and an evaluation of the whole workflow through the design and

implementation of a simple tomosynthesis design with a PBU-50 body phantom. The result of these evaluations demonstrated the feasibility of the workflow.

Finally, it should be noted that the work of this thesis has a clear application in industry, since it is part of a proof of concept of the new generation of radiography systems which will be marketed worldwide by the company SEDECAL.

5.2 Future Work

Even though the main objectives have been fulfilled, further work can still be done, both in improving the proposed workflow and in regards to the application of this workflow.

The simulation and reconstruction tools can be expanded to allow the user to design a wider variety of tomosynthesis protocols. The tomosynthesis module incorporated to the simulation tool during this thesis allows the user to design only tomosynthesis protocols with parallel path geometry (i.e., source and detector move linearly). This module could be updated with the ability to design protocols with other geometries including more complex geometries such as the ones proposed by Zang and Yu [22] in which the source may describe two arcs perpendicular to one another or a zig-zag pattern. In order to make reconstruction possible in these new geometries, appropriate implementations of the Shift-and-Add and Backprojection algorithms would have to be added to the reconstruction tool. This raises the possibility of using systems different from the NOVA FA system used in this thesis such as a C arm.

The acquisition of complete protocols, it can be further automatized. The current implementation involves moving back and forth between the Suspension and Generator interfaces to move the source to the next *autoposition* and to acquire the corresponding projection, respectively. This process could be made easier by creating a new software tool which automatizes the acquisition of complete protocols, hastening the whole workflow.

Finally, the path has now been paved for further research on tomosynthesis by the workflow implemented. This will involve the fine tuning of acquisition and geometric parameters in order to find tomosynthesis protocols tailored for specific systems or even specific parts of the body.

6 Project Management

Time dedicated to the present thesis has been estimated to have been 24 weeks. Each working week corresponds to 20 hours.

6.1 Personnel

The total personnel cost associated with the development of the present project is shown in Table 6.1.

Category	Time (Hours)	Cost/Hour (€)	Cost (€)
Biomedical engineer	480	15	7,200.00
Project coordinator	150	35	5,250.00
Research engineer	200	20	4,000.00
		Total	**16,450.00**

Table 6.1 Personnel cost breakdown

6.2 Material

Table 6.2 displays the material used in the project with a depreciation of 20% at five years.

INVENTORY MATERIALS				
Material	Cost (€)	Cost/Year (€)	Dedication	Cost (€)
Personal computer. AMD Athlon™64 X2 Dual Core Processor 5200+ 2.60 GHz 4,00 GB RAM	1,000.00	200.00	6 months	100.00
GPU: Gigabyte GeForce GTX 660 OC 3GB GDDR5	192.00	38.40	6 months	19.20
Body phantom PBU-50 by Kyoto Kagatu	25,600.00	5,120.00	6 months	2,560.00
			Total	**2,679.20**
FUNGIBLE MATERIALS				
Material				Cost (€)
Phantom: 15 beadings on cork tube				15.00
			Total	**15.00**

Table 6.2 Material cost breakdown

6.3 Other

Concept	Cost (€)	Cost/Year (€)	Dedication	Cost(€)
Matlab programming language license	6,000.00	1,200.00	6 months	600.00
NOVA FA digital radiology system by SEDECAL	50.00€/h		40 hours	2,000.00
			Total	**2,600.00**

Table 6.3 Other costs

6.3 Indirect Cost

Indirect costs are calculated to be 20% of the material and human costs, which is 4,348.80€.

6.4 General Cost & Industrial Benefit

General cost and industrial benefit correspond to the 16% and 6% of the material cost, respectively. Therefore, the general cost is estimated to be 847.07€ and the industrial benefit, 317.65€.

6.5 Total Cost

Aside from personnel, material and indirect cost, the final budget takes into account the 21% VAT.

Concept	Cost (€)
Personnel cost	16,450.00
Total material cost	5,294.20
Other	2,600.00
Indirect cost	1,164.72
Total cost w/o VAT	22,908.92
VAT (21%)	4,810.87
Total	**27,719.79**

Table 6.4 Summary of costs

Therefore, the total budget of this project is:

Total budget: 27,719.79€

Glossary

- **ALARA**: As Low As Reasonably Achievable
- **AP**: Anteroposterior
- **ART**: Algebraic Reconstruction Technique
- **BP**: Backprojection
- **CR**: Computed Radiography
- **CT**: Computed Tomography
- **CUDA**: Computed Unified Device Architecture
- **DBF**: dBASEDatabase File
- **DR**: Direct Radiography
- **FBP**: Filtered Backprojection
- **FDK**: Feldkamp, David and Kreis
- **FOV**: Field of View
- **FRE**: Fiducial Registration Error
- **GPU**: Graphic Processing Unit
- **ICU**: Intensive Care Unit
- **ILTS**: Iterative Least Squares Technique
- **keV**: Kiloelectronvolt
- **kVp**: Kilovoltage Peak
- **LAT**: Lateral
- **LIM**: Laboratorio de Imagen Médica
- **mA**: Milliampere
- **mAs**: Milliampere-Second
- **Matlab**: Matrix Laboratory
- **MITS**: Matrix Inversion Tomosynthesis
- **MLEM**: Maximum Likelihood Expectation Maximization
- **MRI**: Magnetic Resonance Imaging
- **PA**: Posteroanterior
- **PACS**: Picture Archiving and Communication System
- **ROI**: Region of Interest
- **SAA**: Shift-and-Add
- **SART**: Simultaneous Algebraic Reconstruction Technique

- **SDD**: Source-Detector Distance

- **SEDECAL**: Sociedad Española de Electromedicina y Calidad

- **SIRT**: Simultaneous Iterative Reconstruction Technique

- **SOD**: Source-Object Distance

- **SSH**: Secure Shell

- **TAC**: Tomografía Axial Computarizada

- **TACT**: Tuned Aperture Computed Tomography

- **UCI**: Unidad de CuidadosIntensivos

- **VAT**: Value Added Tax

- **VOI**: Volume of Interest

Bibliography

[1] European Space Agency, "ESA - Science & Technology," 23 May 2012. [Online]. Available: http://sci.esa.int/jump.cfm?oid=50368. [Accessed Jul 2016].

[2] Antonine Education, [Online]. Available: http://www.antonine-education.co.uk/Pages/Physics_5_Options/Medical_Physics/MED_07/med_phys_7.htm. [Accessed Jul 2016].

[3] J. Beutel, H. L. Kundel and R. L. Van Metter, Handbook of Medical Imaging: Physics and psychophysics, SPIE Press, 2000.

[4] "Scientific Sentence," 2010. [Online]. Available: http://scientificsentence.net/Radiations/index.php?key=yes&Integer=attenuation. [Accessed Jul 2016].

[5] M. M. Körner, C. H. M. Weber, S. M. Wirth, K.-J. M. Pfeifer, M. F. M. Reiser and M. M. Treitl, "Advances in Digital Radiography: Physical Principles and System Overview," *RadioGraphics,* vol. 27, no. 3, pp. 675-686, 2007.

[6] B. Mathiszik, "EDN Network," EDN, Aug 2005. [Online]. Available: http://www.edn.com/Home/PrintView?contentItemId=4382009. [Accessed Jul 2016].

[7] M. Fernanda and N. Albarran, "Estudios radiológicos en pediatría," 2014. [Online]. Available: http://estudiosradiologicosdepediatria.blogspot.com.es/p/proyecciones-y-posiciones-radiologicas.html. [Accessed Jul 2016].

[8] Saúde, Doenças e Medicina, "saudemedicina," [Online]. Available: http://www.saudemedicina.com/tomografia/. [Accessed Jul 2016].

[9] E. F. Conant, E. F. Beaber, B. L. Sprague, S. D. Herschorn, D. L. Weaver, T. Onega, A. N. Tosteson, A. M. McCarthy, S. P. Poplack, J. S. Haas, K. Armstrong, M. D. Schnall and W. E. Barlow, "Breast cancer screening using tomosynthesis in combination with digital mammography compared to digital mammography alone: a cohort study within the PROSPR consortium," *Breast Cancer Research and Treatment,* vol. 156, no. 1, pp. 109-116, Febuary 2016.

[10] T. M. Svahn, D. P. Chakraborty, D. Ikeda, S. Zackrisson, Y. Do, S. Mattsson and I. Andersson, "Breast tomosynthesis and digital mammography: a comparison of diagnostic accuracy," *The British Journal of radiology,* vol. 85, no. 1019, pp. e1074-e1082, 2012.

[11] K. R. Brandt, D. A. Craig, T. L. Hoskins, T. L. Henrichsen, E. C. Bendel, S. R. Brandt and J. Mandrekar, "Can Digital Breast Tomosynthesis Replace Conventional Diagnostic

Mammography Views for Screening Recalls Without Calcifications? A Comparison Study in a Simulated Clinical Setting," *Americal Journal of Roentgenology,* vol. 200, no. 2, pp. 291-298, 2013.

[12] S. Ciatto, N. Houssami, D. Bernardi, F. Caumo, M. Pellegrini, S. Brunelli, P. Tuttobene, P. Bricolo, C. Fantò, M. Valentini, S. Montemezzi and P. Macaskil, "Integration of 3D digital mammography wih tomosynthesis for population breast-cancer screening (STORM): a prospective comparison study," *The Lancet Oncology,* vol. 14, no. 7, pp. 583-589, 2013.

[13] T. Gomi, M. Nakajima, H. Fujiwara, T. Takeda, K. Saito, T. Umeda and K. Sakaguchi, "Comparison between chest digital tomosynthesis and CT as a screening method to detect artificial pulmonary nodules: a phantom study," *The Britis ournal of Radiology,* vol. 85, no. 1017, pp. e622-e629, 2012.

[14] J. Vikgren, S. Zachrisson, A. Svalkvist, A. A. Johnsson, M. Boijsen, A. Flinck, S. Kheddache and M. Bath, "Comparison of Chest Tomosynthesis and Chest Radiography for Detection of Pulmonary Nodules: Human Observer Study of Clinical Cases," *Radiology,* vol. 249, no. 3, pp. 1034-1041, December 2008.

[15] J. Hsieh, "Conventional X-Ray Tomography," in *Computed Tomography: Principles, Design, Artifacts, and Recent Advances*, SPIE Press, 2003, p. 2.

[16] J. T. Dobbins III and D. J. Godfrey, "Digital x-ray tomosynthesis: current state of the art," *Physics in Medicine and Biology,* vol. 48, pp. R65-R106, 2003.

[17] H. Machida, T. Yuhara, T. Mori, E. Ueno, Y. Moribe and J. M. Sabol, "Optimizing Parameters for Flat-Panel Detector Digital Tomosynthesis," *RadioGraphics,* vol. 30, pp. 549-562, 2010.

[18] J. T. Dobbins III and H. P. McAdams, "Chest tomosynthesis: Technical principles and clinical update," *European Journal of Radiology,* pp. 244-251, 2009.

[19] L. T. Niklason, B. T. Christian, L. E. Niklason, D. B. Kopans, D. E. Castleberry, B. H. Opsahl-Ong, C. E. Landberg, P. J. Slanetz, A. A. Giardino, R. Moore, D. Albagli, M. C. DeJule and Fitzger, "Digital Tomosynthesis in Breast Imaging," *Radiology,* vol. 205, pp. 399-406, 1997.

[20] I. Sechopoulos, "A review of breast tomosynthesis. Part I. The image acquisition process," *Medical Physics,* vol. 40, 2013.

[21] D. Xia, S. Cho, J. Bian, E. Y. Sidky, C. A. Pelizzari and X. Pan, "Tomosynthesis with Source Positions Distributed over a Surface," in *Proc. SPIE 6913, Medical Imaging 2008: Physics of Medical Imaging, 69132A (March 18, 2008)*.

[22] J. Zang and C. Yu, "A novel solid-angle tomosynthesis (SAT) scanning scheme," *Medical Physics,* vol. 37, no. 8, pp. 4186-4192, 2010.

[23] J. G. Mainprize, A. K. Bloomquist, M. P. Kempston and M. J. Yaffe, "Resolution at oblique incidence angles of a flat panel imager for breast tomosynthesis," *Medical Physics,* vol. 33, no. 9, pp. 3159-3164, 2006.

[24] Z. Kolitski, G. Panayiotakis, V. Anastassopoulos, A. Scodras and N. Pallikarakis, "A multiple projection method for digital tomosynthesis," *Med Phys,* vol. 19, no. 4, pp. 1045-1050, 1992.

[25] R. L. Webber, R. A. Horton, D. A. Tyndall and J. B. Ludlow, "Tuned-aperture computed tomography (TACT). Theory and application for three-dimensional dento-alveolar imaging," *Dentomaxillofacial Radiology,* vol. 26, pp. 53-62, 1997.

[26] J. T. Dobbins III, "Tomosynthesis imaging: At a translational crossroads," *Medical Physics,* vol. 36, no. 6, pp. 1956-1967, 2009.

[27] I. Sechopoulos, "A review of breast tomosynthesis. Part II. Image reconstruction, processing and analysis, and advanced applications," *Medical Physics,* vol. 40, 2013.

[28] L. A. Feldkamp, L. C. Davis and J. W. Kress, "Practical cone-beam algorithm," *J. Opt. Soc. Am.,* vol. 1, no. 6, pp. 612-619, 1984.

[29] J. C. Park, S. H. Park, J. S. Kim, Y. Han, M. K. Cho, H. K. Kim, Z. Liu, S. B. Jiang, B. Song and W. Y. Song, "Ultra-Fast Digital Tomosynthesis Reconstruction Using General-Purpose GPU Programming for Image-Guided Radiaton Therapy," *Technology in Cancer Research and Treatment,* vol. 10, no. 4, pp. 295-306, 2011.

[30] D. N. Ghosh Roy, R. A. Kruger, B. Yih and P. Del Rio, "Selective plane removal in limited angle tomographic imaging," *Medical Physics,* vol. 12, no. 65, pp. 65-70, 1985.

[31] J. T. Dobbins III, A. O. Powell and Y. K. Weaver, "Matrix Inversion Tomosynthesis: initial image reconstruction," in *RSNA 73rd scientific assembly*, 1987.

[32] J. G. Colsher, " Iterative three-dimensional image reconstruction from tomographic projections," *Computer Graphics and Image Processing,* vol. 6, pp. 513-537, 1977.

[33] A. H. Andersen and A. C. Kak, "Simultaneous algebraic reconstruction technique (SART): a superior implementation of the art algorithm," *Ultrasonic Imaging,* vol. 6, no. 1, pp. 81-94, 1984.

[34] T. Wu, R. H. Moore, E. A. Rafferty and D. B. Kopans, "A comparison of reconstruction algorithms for breast tomosynthesis," *Medical Physics,* vol. 31, no. 9, pp. 2636-2647, 2004.

[35] Y. Zhang, H.-P. Chan, B. Sahiner, J. Wei, M. M. Goodsitt, L. M. Hadjiiski, J. Ge and C. Zhou, "A comparative study of limited-angle cone-beam reconstruction," *Medical Physics,* vol. 33, no. 10, pp. 3781-3795, 2006.

[36] T. Deller, K. N. Jabri, J. M. Sabol, X. Ni and e. a. Gopal Avinash, "Effect of acquisition parameters on image quality in digital tomosynthesis," *Proceedings of SPIE,* vol. 6510, 2007.

[37] Á. Martínez, A. García-Santos, I. García, E. Serrano, J. García, C. de Molina, R. Polo, M. Desco and M. Abella, "A software tool for the design and simulation of X-ray acquisition protocols," *Unpublished,* 2016.

[38] T. Mertelmeier, J. Ludwig, B. Zhao and B. Zhao, "Optimization of Tomosynthesis Acquisition Parameters: Angular Range and Number of Projections," in *Digital Mammography: 9th International Workshop, IWDM 2008 Tucson, AZ, USA, July 20-23, 2008 Proceedings*, Berlin, Heidelberg, Springer Berlin Heidelberg, 2008, pp. 220-227.

[39] M. Bissonnette, M. Hansroul, E. Masson, S. Savard, S. Cadieux, P. Warmoes, D. Gravel, J. Agopyan and B. Polischuk, "Digital breast tomosynthesis using an amorphous selenium flat panel detector," *Proceedings of SPIE,* vol. 5745, no. 1, pp. 529-540, 2005.

[40] D. Kontos, C. Zhang, N. Ruiter, P. R. Bakic and A. D. Maidment, "Evaluating the Effect of Tomosynthesis Acquisition Parameters on Image Texture: A Study on an Anthropomorphic Breast Tissue Software Model," in *Digital Mammography, 9th International Workshop, IWDM 2008*, Tucson, AZ, USA, July 20-23, 2008.

[41] G. Lee, Y. J. Jeong, K. I. Kim, J. W. Song, D. M. Kang, Y. D. Kim and J. W. Lee, "Comparison of chest digital tomosynthesis and chest radiography for detection of asbestos related pleuropulmonary disease," *Clinical Radiology,* vol. 68, no. 4, pp. 376-382, 2013.